Draft version December 14, 2025
Typeset using LaTeX **twocolumn** style in AASTeX7.0.1

Expanding Asteroseismic Studies in Star Clusters Using NASA's TESS and ESA's Gaia Missions

Carli Mankowski[1], Jamie Tayar[1] and Cassidy Martin[1]

[1]*Department of Astronomy, University of Florida, Gainesville, FL 32611, USA*

ABSTRACT

Star clusters have long been central to the study of stellar evolution due to their chemically and chronologically homogeneous populations. Asteroseismology, the analysis of stellar oscillations and pulsations, provides precise information about properties such as masses, radii, and ages of stars in the field. However, these stars lack calibration to an absolute scale, and so this project seeks to utilize the data from NASA's *TESS* mission and ESA's *Gaia* mission to identify additional cluster stars suitable for asteroseismic analysis and calibration. In this work we analyze 14 stars belonging to 3 well-populated clusters, 5 additional stars that are the only detected oscillators in their respective clusters, and 3 detected oscillators of unknown cluster membership. By nearly doubling the number of clusters with measured oscillating giants, this project increases the opportunity for cross-validation between classical stellar models and asteroseismic methods, allowing for improvements in both calibration techniques and age estimations across the galaxy.

Keywords: Asteroseismology — Stellar oscillations — Open star clusters — Stellar evolutionary models — Stellar photometry — Stellar properties — *Gaia* — Stellar pulsations

1. INTRODUCTION

The determination of stellar age is foundational in our understanding of galactic formation. In order to accurately infer stellar ages, we need to be able to calibrate models using well-studied examples and observed data. Increasing our understanding of the relationship between stellar properties and age enables connections across diverse areas of astronomy. Ages can be combined with chemical diagnostics (J. J. Cowan et al. 2025), nucleosynthetic pathway studies (G. Casali et al. 2022) and large-scale kinematic maps (S. Buder et al. 2021) to help reconstruct the Milky Way's history. They also enhance chemical evolution models, improve stellar mass estimates, and inform other observational analyses (D. Stello & S. Sharma 2023). Its large-scale applicability and long-standing academic scrutiny secures stellar age as a cornerstone diagnostic element of galactic study. Examples of the contextual applicability of stellar age include the topics of planetary system evolution (J.-Y. Yang et al. 2023), galaxy mergers (D. Horta et al. 2024), galactic chemical enrichment (D. K. Feuillet et al. 2018), and epochs of star formation (D. Thomas et al. 2005). Our very understanding of the Milky Way is a prime example of the integration of age estimations and observational constraints (i.e., photometric, spectroscopic, and kinematic diagnostics). Using the ages of galactic globular clusters allows us to study early formation; using the ages of non-primordial clusters allows us to study our galaxy's accretion events from long ago (J. M. Ying et al. 2025). In this way, stellar age serves as a unifying metric for individual stellar histories and the evolution of stellar, galactic, and cosmological studies.

Star clusters have long been central to the study of stellar evolution because their chemically and chronologically homogeneous populations make them ideal laboratories for testing and calibrating age estimates and other theoretical models. This remains true across a diverse sample of masses and evolutionary stages (A. Miglio et al. 2021b). Using known models such as Color Magnitude Diagrams (CMDs) (T. Cantat-Gaudin & F. Anders 2020) and isochrone fitting (C. Reyes et al. 2024) can also aid in the determination of stellar properties across this same wide-scale sample. Although star clusters have long served as key laboratories for testing and calibrating stellar-evolution and age-dating models, the majority of observable stars reside outside of bound clusters. Calibrating these models on cluster members then enables their application to field stars whose ages cannot be independently confirmed. Recent advances in asteroseismology have demonstrated the potential to infer ages for hundreds of thousands of field stars if their accuracy can be anchored to coeval benchmarks such as clusters (M. Hon et al. 2024; A. T. Theodoridis et al. 2025).

Asteroseismology is the study of stellar oscillation for the purpose of gaining insight into internal stellar structure (T. M.

Email: carli.mankowski@ufl.edu

Brown et al. 1989; H. Kjeldsen & T. R. Bedding 1995). Characterizing the frequencies of these resonant oscillations in solar-like oscillators provides insight into various properties such as stellar evolution (W. J. Chaplin & A. Miglio 2013), stellar mass, radii, and luminosity (S. Hekker et al. 2011). Defining global asteroseismic observables include $\Delta\nu$, the large frequency separation between overtone modes of the same angular degree, and $\nu_{\rm max}$, the frequency at which the oscillation power envelope reaches its maximum (S. Hekker et al. 2011).Oscillatory behavior is closely correlated with stellar mass and radius (A. L. Ash et al. 2024). Using asteroseismology with scaling relations (M. Hon et al. 2024) allows for accurate age estimation and is thus a gateway for quantitative progress in understanding stellar history and evolutionary timescales (Y. Lebreton & J. Montalbán 2008).

At this point, a variety of space-based photometry missions have provided the necessary data to characterize the asteroseismic oscillations of thousands of stars, and almost all of them have included subsets of stars in clusters that can be used for calibration. CoRot (COnvection, ROtation and planetary Transits) (2006–2013) (A. Baglin et al. 2006) pioneered space-based asteroseismology by detecting thousands of red giant oscillations among solar-like stars (B. Mosser et al. 2018), and the *Kepler* mission (2009–2013) (W. J. Borucki et al. 2010) subsequently revealed tens of thousands more oscillators in a similar stellar sample (J. Yu et al. 2018). The K2 campaign (2014–2018) (S. B. Howell et al. 2014) included cluster members, giants, and a few dwarf stars through thousands of detections (J. C. Zinn et al. 2022), while *TESS* (2018–present) (G. R. Ricker et al. 2015) has surveyed the bright all-sky field and identified over 158,000 oscillators, predominantly red giants (M. Hon et al. 2021).

Combining asteroseismology with supplemental information such as *Gaia* photometry (S. Risbud et al. 2025; J. Donor et al. 2023) and cluster membership (E. L. Hunt & S. Reffert 2023; J. Tayar & M. Joyce 2025) can expand the impact of asteroseismology and constrain the chemical and dynamical evolution of stars; integration of these large, consistent datasets allows for deeper comparative analysis. However, their age estimations are still at odds with those derived from isochrone fitting (J. Tayar & M. Joyce 2025; D. B. Palakkatharappil & O. L. Creevey 2023).

In this context, NASA's *TESS* mission, launched on 2018 April 18, provides nearly all-sky high-precision photometry. *TESS* operates in a 27.4-day highly elliptical Earth orbit, observing consecutive ($24^\circ \times 96^\circ$) sectors (G. R. Ricker et al. 2015) and delivering both light curves and full-frame images (FFIs) (K. G. Stassun et al. 2019b), ultimately achieving continuous coverage of more than 95% of the sky (J. M. Jenkins et al. 2016). We can now also advance asteroseismic studies using *TESS* data due to its all-sky coverage of many targets with high precision. Since *TESS* provides asteroseismic data for solar-type stars (G. R. Ricker et al. 2015) all over the sky, it opens the possibility of greatly increasing the number of clusters with asteroseismic data that could then be used to calibrate the ages of hundreds of thousands of oscillators across the galaxy.

However, the fundamental operation of *TESS* can impose certain limitations that can impair the study of asteroseismology. Since *TESS* has a large pixel size, light from nearby sources can impose on that of target stars, especially in crowded fields, complicating the extraction of clean light curves for individual stars (E. Hatt et al. 2023). Additionally, upon its initial launch, *TESS*'s 30-minute cadence imposed a Nyquist frequency limit of 278 μHz: the highest frequency that can be accurately sampled without aliasing, which may affect the asteroseismology of stars with oscillation frequencies at or around that Nyquist limit (S. J. Murphy 2015; T. Barclay et al. 2020). *TESS* also faces analytical limitations, including lost detections caused by data gaps and short observing sectors (N. M. Guerrero et al. 2021) and challenges arising from its month-to-month discontinuous observing pattern (Y. Lu et al. 2020).

Therefore, to promote the efficient analysis of *TESS* asteroseismology in star clusters, we aim to establish a database of cluster stars that are suitable for seismic analysis, even with the limitations of the *TESS* mission as described above. For example, we are interested in whether the ages derived from global asteroseismic parameters are consistent with cluster ages obtained from isochrone fitting. Previous work has suggested that seismically inferred ages may differ systematically from those obtained using other techniques, often yielding larger values (J. Tayar & M. Joyce 2025). However, the small number of clusters analyzed to date, together with their limited coverage in metallicity and age, makes it difficult to assess the true accuracy and precision of ages inferred from asteroseismology.

In this study we combine precise astrometry, membership information, and isochrone-based ages for nearby open clusters from the *Gaia* mission with all-sky photometric data from *TESS*. We demonstrate that, despite the relatively short time series and large pixel scale of *TESS*, its data are sufficient in many cases to characterize the oscillations of red giant cluster members. We then compare ages inferred from asteroseismic scaling relations and stellar age modeling to literature cluster parameters in order to map the reliability of seismic ages, enabling their broader application to infer the ages of large samples of field stars across the Milky Way (A. T. Theodoridis et al. 2025). To facilitate future work, we provide a catalog of cluster stars that may be suitable for seismic analysis with *TESS*.

2. METHODS

2.1. *Catalog Selection*

The foundation of this work relies on careful characterization and association of cluster stars. We use *Gaia* DR3, whose all-sky parallaxes, proper motions, magnitudes, BP-RP colors, and other photometry allow for accuracy in determining open-cluster membership, precise distances, and clean HR-diagram placement (Gaia Collaboration et al. 2023). This photometric data is pulled from cluster membership studies such as E. L. Hunt & S. Reffert (2023), R. P. Schiavon et al. (2023), and T. Cantat-Gaudin & F. Anders (2020), which have already grouped members of the same clusters together with reasonable confidence.

Using the E. L. Hunt & S. Reffert (2023), R. P. Schiavon et al. (2023), and T. Cantat-Gaudin & F. Anders (2020) catalogs, we queried the *TESS* Input Catalog (TIC v8; K. G. Stassun et al. 2019b) via the S3 STScI public dataset using `astroquery.mast.cloud` to isolate targets with unique TIC IDs. To account for systematic errors such as field variation, cosmic noise, and electro-optical response differences (M. Gai et al. 2022), the right ascension and declination of each target were given a radial error window of 0.1 degrees. After confirming that each target was present in the *TESS* Input Catalog, we performed a column-wise merge to match E. L. Hunt & S. Reffert (2023), R. P. Schiavon et al. (2023), and T. Cantat-Gaudin & F. Anders (2020) members with a CSV file containing TIC IDs from the 2019 TIC-7 Input Catalog (K. G. Stassun et al. 2019a). These two datasets were merged on a shared identifier column (*Gaia* DR3), producing a functional catalog of stars with secure membership classifications and relevant astrometry. This catalog contains 38311 members for further consideration, all within the *TESS* input catalog.

2.2. *Distance Cuts*

We filter our catalog to eliminate distant targets, following the findings of T. Cantat-Gaudin & F. Anders (2020), which concluded that *Gaia* DR3 proper motion uncertainties contribute at ~500 pc and dominate at distances beyond 1000 pc. Using the identity $d = \frac{1000}{\varpi}$, where d is the distance in parsecs and ϖ is the parallax in milliarcseconds, we use catalog-provided parallax data to remove any stars at distances greater than 1 kpc. This reduces the systematic noise and measurement uncertainty from the dataset. Filtering out distant stars leaves a nearby sample with more reliable absolute magnitudes, because parallax-based distance uncertainties and absolute-magnitude uncertainties are typically a factor of $\sim$ 5–10 smaller for stars within a few kiloparsecs than for more distant objects (L. Lindegren et al. 2018).

2.3. *Magnitude Filtering*

We take into consideration the intense “bleeding” effect of bright stars on *TESS*’s camera in the creation of our catalog. Stars that are exceptionally bright will not yield any photometric data, as the *TESS* pipeline does not process anything past its brightness threshold (TESS Science Processing Operations Center 2025). For targets under that threshold, we cannot extract reliable brightness data from stars whose light bleeds into multiple pixels, introducing the need for a “cap” on how bright a star can be. This is explored further in section §2.5. We use the *TESS* QLP Aperture Lightcurve Products, which are generated only for stars brighter $T \approx 13.5$ and can exclude the very brightest targets when bleed-trail pixel stamps preclude standard processing (MIT TESS Science Office 2025; M. Fausnaugh & the TESS Team 2023).

We also account for the increased contamination and background noise affecting fainter *TESS* targets, which becomes a significant issue beyond $G \sim 15$ and renders stars fainter than $G \gtrsim 16$ largely unsuitable for precise asteroseismology (M. Riello et al. 2021; A. W. Boyle et al. 2025). Following previous asteroseismic work and K. G. Stassun et al. (2019c), we restrict our sample to stars with $G \leq 13$ mag so solar-like oscillations can be reliably detected at high signal-to-noise and to prioritize high signal-to-noise targets for analysis (M. Hon et al. 2021; A. W. Boyle et al. 2025; J. Zhou et al. 2024; S. Grusnis et al. 2025).

2.4. *Color Magnitude Diagrams and Red Giant Selection*

We require all stars in our sample to have reported *Gaia* photometry (G and $G_{\rm BP} - G_{\rm RP}$). To obtain these values, we merge the cluster member list with the *Gaia* DR3 photometric catalog of R. Andrae et al. (2023). This addition allows us to construct a color–magnitude diagram (CMD) that traces the evolutionary state of each star (Gaia Collaboration et al. 2018). Following the methods of T. Konchady (2020), we create a CMD from the mean G-band magnitude (G) and color index ($G_{\rm BP} - G_{\rm RP}$) provided by the XGBoost-based *Gaia* DR3 catalog. In our analysis, this XGBoost catalog is used for the photometry and atmospheric parameters ($T_{\rm eff}$, [Fe/H], and $\log g$). Where these values are missing or physically unrealistic, we use atmospheric parameters adopted from the `gspec` spectroscopic catalog. By applying the distance modulus,

$$M_G = G - 5\log_{10}(d) + 5, \tag{1}$$

we convert all of the Gmag values in the catalog (G) into the absolute magnitude M_G.

This catalog follows the selection principles of M. Hon et al. (2022) and R. A. García et al. (2022), prioritizing red giants because their solar-like oscillations have larger amplitudes and are detected at higher rates in *TESS* data. Since red giants span a broad range of stellar ages (M. Xiang et al. 2023), this should allow us to test the reliability of seismically inferred ages more generally. We visualize the full sample on a *Gaia*-based CMD (Figure 1) and we also show the three most populated clusters with seismic detections in our sample, Casado Alessi-1, Theia 6046, and NGC 752 (Figure 2). We approximate the location of the main sequence in this diagram in order to exclude stars that are unlikely to be red giants. To do this, we define an empirical main-sequence locus in color–magnitude space and remove stars that fall close to this sequence rather than on the red giant branch. The main sequence line used in our CMD approximation is given by $M_G = 3.5 \times (BP - RP)$ where M_G is the absolute *Gaia* G-band magnitude and $BP - RP$ is the *Gaia* color index. In order to be fairly confident that our sample only contains red giants, we filter this CMD so that each target greater than 3.5 units of magnitude away from the main sequence line in the $+y$ direction is deemed a potential red giant. Out of the initial sample of 38,311 distance and magnitude corrected stars, 986 are estimated to be potential red giants and the other 37,667 are estimated to be potential main sequence.

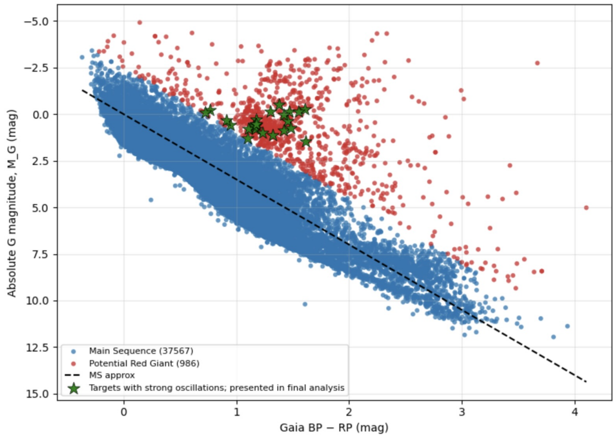

Figure 1. Global HR diagram using (*Gaia*) absolute magnitude vs BP-RP color, with the location of the Main Sequence approximated by the dashed line.

2.5. *Crowding, Bleeding and Duration Requirements*

TESS's observing pattern, large pixels, and susceptibility to saturation around the brightest stars can result in a degradation of data quality that makes seismic analysis challenging or impossible. This suggests that not every cluster red giant in our sample will have the quality of data needed to perform asteroseismology. For this analysis, we want to focus on stars with clean point-spread functions and sufficient data. To address this, we individually inspect each potential star to ensure the *TESS* data exists. Then, we check if nearby stars allow for the extraction of a clean light curve, or if local saturation and bleeding would result in the need for more advanced light curve techniques (B. J. S. Pope et al. 2016). Specifically, we used each star's right ascension (RA), declination (Dec), and *Gaia* DR3 name to create a 10x10 pixel cutout around each target star using NASA's Timeseries Integrated Knowledge Engine (TIKE). Nearby bright neighbors present the possibility for contaminated light-curves; we identified extraneous stars within both 3 magnitudes and 2 arcminutes of our target. We marked those nontarget stars to evaluate potential contamination of seismic signals.

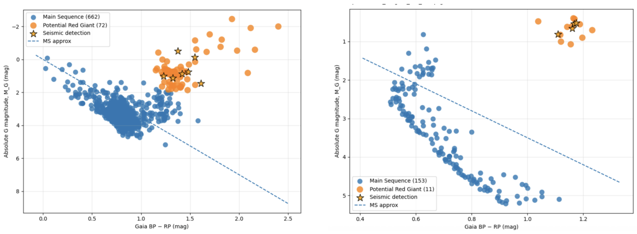

(a) Theia_6046 (b) NGC_752

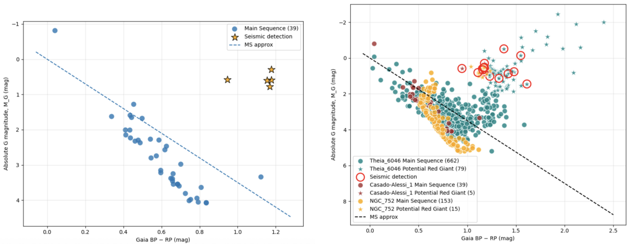

(c) Casado Alessi-1 (d) Three–cluster overlay

Figure 2. Cluster HR diagrams for the three clusters in our study with more than one seismic detection in a giant.

For each star in our sample, we compiled individual identification information as well as visual inspection ratings into a table. Ratings were allocated to each target using a 1 to 5 scale with 5 representing the cleanest data. Several stars had no available sectors, these are marked with "-1" in the table and are not considered for further analysis. To create these visualizations, the first available sector was used. Exceptions were made for scenarios in which the target was either excessively faint or on the edge of the detector, and the next suitable sector was used. In Figure 3, we show representative cutouts with fixed bleeding and varying levels of crowding, and the impact of varying bleeding values at fixed crowding levels. Our full table of results is available on Zenodo, and the code to generate these cutouts can be found here.

We restricted our sample to stars with bleeding and crowding values of at least 2 and at least five available sectors. Only this subset of red giants was used in the subsequent analysis, though results for all targets are provided for reference and to enable future work. All quality cuts up to this point are replicable and the process is outlined on GitHub.

2.6. *TESS Light Curve Retrieval and Pre-Processing*

We then retrieved the raw light curves for the targets that had adequate bleeding, crowding, and sector metrics. Using the `lk.search_lightkurve` function, we located each *TESS* light curve from the QPL pipeline and downloaded For each sector, we normalized and flattened the data with

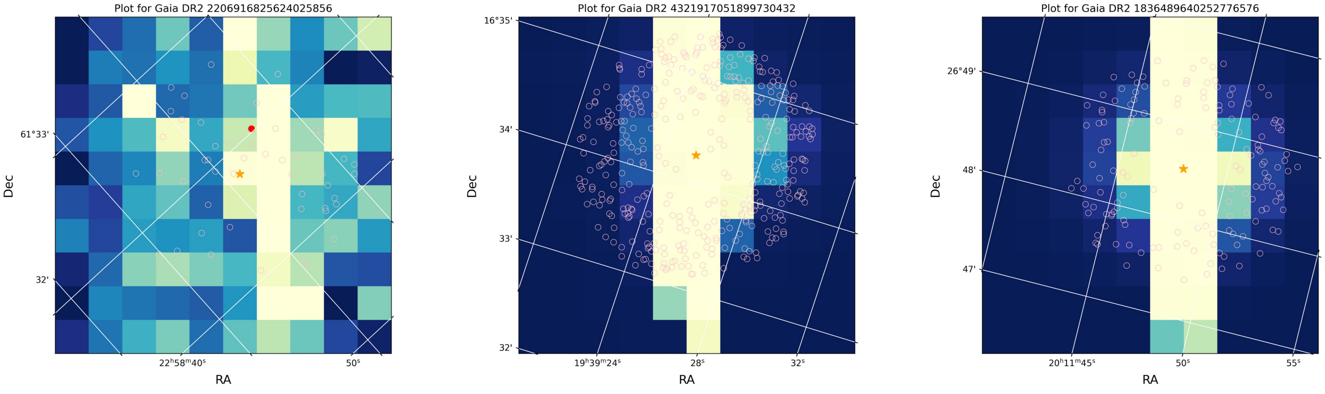

(a) Bleeding = 1, Crowding = 1 (b) Bleeding = 1, Crowding = 4.5 (c) Bleeding = 1, Crowding = 5

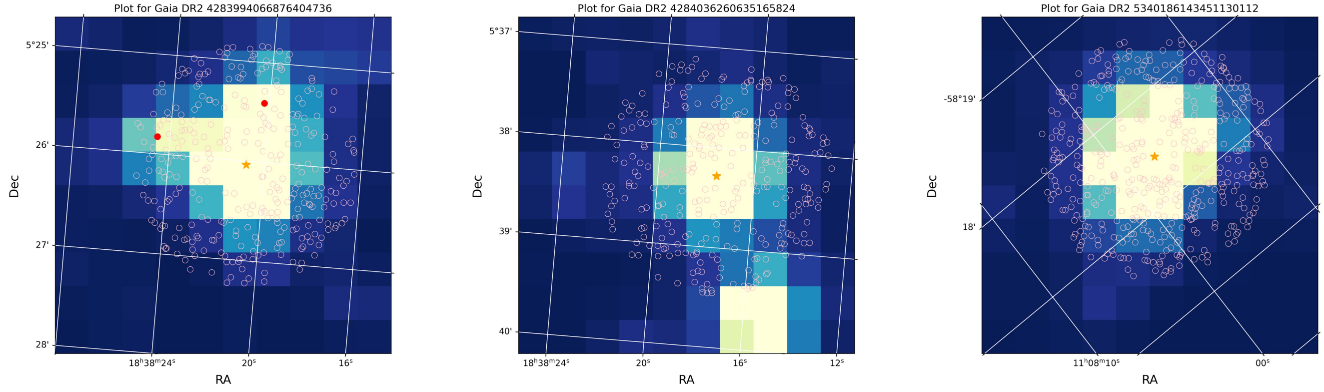

(d) Bleeding = 3, Crowding = 1 (e) Bleeding = 3, Crowding = 3 (f) Bleeding = 3, Crowding = 5

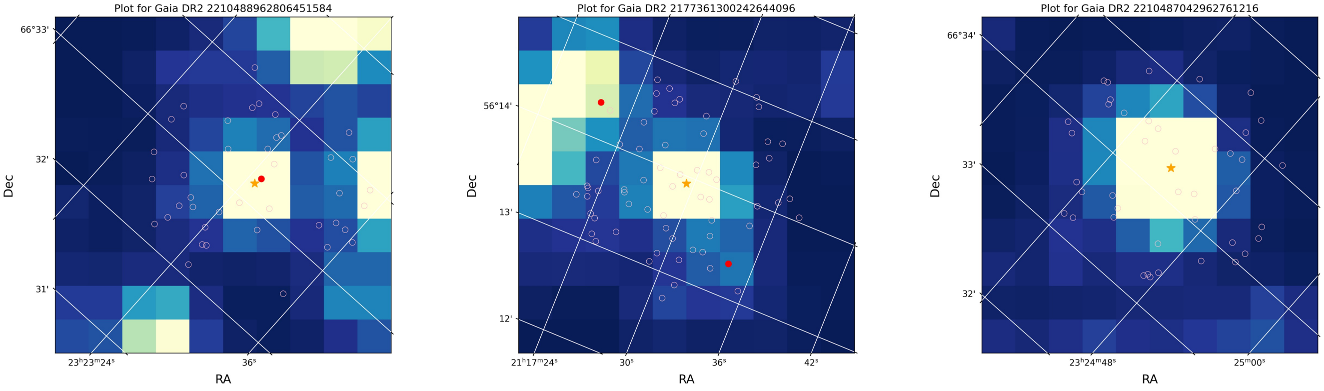

(g) Bleeding = 5, Crowding = 1 (h) Bleeding = 5, Crowding = 3 (i) Bleeding = 5, Crowding = 5

Figure 3. Nine-panel grid of *TESS* targets across various bleeding (grouped horizontally) and crowding (grouped vertically) ratings.

a 299-cadence window, and removed 2.75σ outliers. We then stitched all available sectors into a single light curve and sorted the points by time (J. M. Jenkins et al. 2016). To avoid large gaps between sectors in the analysis, whenever we encountered a gap larger than 10 days in the time array, we subtracted the size of that gap from all subsequent time stamps so that the combined light curve formed a continuous time series. As suggested in M. N. Lund et al. (2021), this pre-processing is an essential prerequisite to *TESS* data analysis, since the high values of systematic noise can damage results. The light curves were converted into power spectra, oversampled by a factor of five to achieve a frequency resolution of $\sim 0.1\,\mu$Hz. The spectra were binned, using five-point binning for $\nu_{\rm max}$ estimation and 25-point binning for background fitting, following methods presented in A. Chontos et al. (2022b).

2.7. *PySYD Seismic Analysis*

Using PySYD, an open-sourced Python adaptation of the SYD method, we aimed to have code auto detect the asteroseismic parameters $\nu_{\rm max}$ and $\Delta\nu$. As noted in D. Huber et al. (2009), the underlying SYD methodology was commonly used to measure oscillatory parameters in *Kepler* stars. Extending this to *TESS*, we needed to neutralize the noisy data with Gaussian smoothing of the oscillation power excess, an approach motivated by D. Huber et al. (2009) and justified by M. Hon et al. (2022). We set 50 Monte Carlo iterations, restrict $\nu_{\rm max}$ to 1–100 μHz initially, refine the power spectrum to 10–60 μHz, and fit the background between 5–525 μHz. Running PySYD produced $\nu_{\rm max}$ (See Figure 4) and $\Delta\nu$ estimates, background model fits, uncertainties, and diagnostic plots. Window restrictions were adjusted appropriately for each target, and uncertainties for $\nu_{\rm max}$ were calculated considering both PySYD values and visual inspection, referring to how far in each direction can be feasibly interpreted as $\nu_{\rm max}$. Our typical fractional uncertainty on $\nu_{\rm max}$ is 3.3%, comparable to the APOKASC-3 values reported by M. H. Pinsonneault et al. (2025).The Jupyter notebook used to run this PySYD analysis is openly available on GitHub.

2.8. *Échelle Diagram Construction and Validation*

To ensure that we report the most accurate $\Delta\nu$ values, we created two different interactive Échelle diagrams: a 2D heatmap and a collapsed ridge alignment strip (See Figure 5), using the D. Hey & W. Ball (2020) code as a base and starting point. These all operate within a $\pm 2\Delta\nu$ window around $\nu_{\rm max}$ and are adjustable using a Bokeh package Custom JavaScript (JS) slider which instantaneously populates the graph with $\Delta\nu$ values as the slider is manipulated. Each target was passed through both plots, inspected, and the best $\Delta\nu$ was recorded along with more accurate uncertainties, referring to how far in each direction can be feasibly interpreted as $\Delta\nu$. Our typical fractional uncertainty on $\Delta\nu$ is 2.26% , comparable to the APOKASC-3 values reported by M. H. Pinsonneault et al. (2025). The Jupyter notebook used to produce all Échelle figures and $\Delta\nu$ estimates is openly available on GitHub.

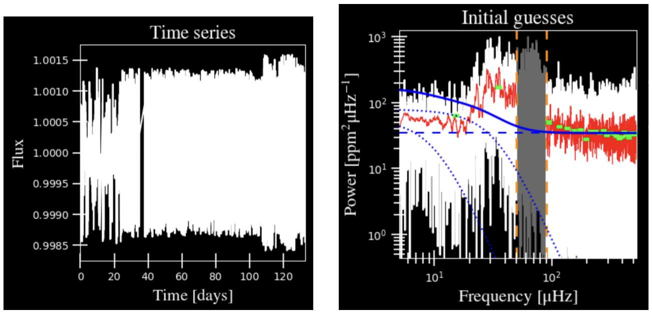

(a) Time series (b) Initial guesses

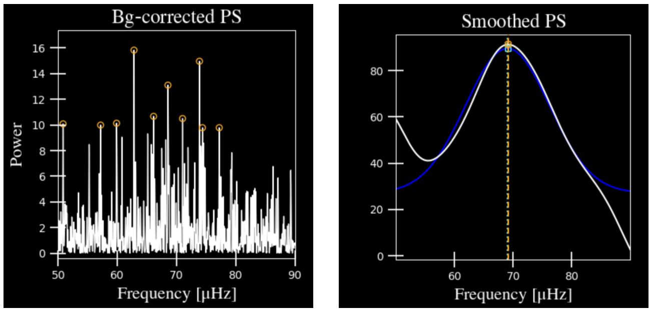

(c) Bg-corrected PS (d) Smoothed PS

Figure 4. Summary of the background fitting and $\nu_{\rm max}$ measurement for TIC 306955660. Panel (a) shows the detrended time series, (b) the initial background model components, (c) the background–corrected power spectrum, and (d) the smoothed power spectrum with the vertical dashed line marking the peak at $\nu_{\rm max}$.

2.9. *Evolutionary State Determination, Corrections, and Scaling Relations*

In order to apply the appropriate corrections to the $\Delta\nu$ estimates, we first identified the evolutionary state of each star. While in some cases it is possible to infer the evolutionary state directly from the oscillations(B. Mosser et al. 2012; M. Vrard et al. 2025; Y. Elsworth et al. 2019), this is challenging in low signal to noise cases like our data. Therefore, we infer evolutionary states from the *Gaia* color-magnitude diagram here, although future work may be able to improve upon this looking at each cluster in detail. Using the *Gaia* color–magnitude diagram, we tagged stars as red clump (RC) if they lay within a conservative rectangular region centered on the RC overdensity, using `RC_COLOR_MIN, RC_COLOR_MAX = 0.9, 1.3` in $(BP - RP)$ and `RC_MG_MIN, RC_MG_MAX = 0.2, 1.0` in M_G. *Gaia*'s *FLAME* radii are the stellar radii estimated by the *Gaia* DR3 *FLAME* module, which combines bolometric fluxes, effective temperatures, and parallaxes (Gaia Collaboration 2022), and has been used for population studies (R. Andrae et al. 2023). Applying the same selection box to an M67 *Gaia* CMD constructed from *FLAME* radii

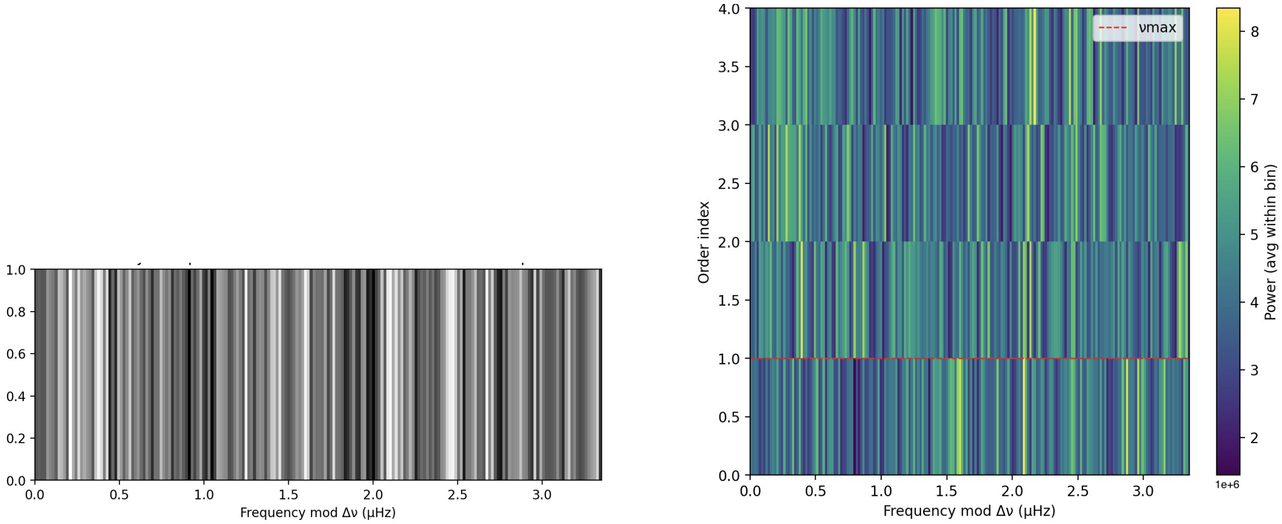

(a) Overlay collapsed échelle

(b) 2D échelle ($\pm 2\Delta\nu$ around $\nu_{\rm max}$)

Figure 5. Échelle diagnostics for TIC 306955660 with input large separation $\Delta\nu = 3.350$ μHz. Panel (a) shows the overlay-style collapsed échelle (frequency modulo $\Delta\nu$). Panel (b) shows the 2D échelle; the dashed line marks $\nu_{\rm max}$.

shows that it also cleanly traces the observed RC overdensity in that open cluster and shows that our cuts are consistent with well-behaved benchmark populations (Figure 6). We feel this box is an appropriate approximation for the compact RC feature near $(BP-RP) \approx 1.1$ and $M_G \approx 0.6$ visible in *Gaia* DR3 HRDs (Gaia Collaboration et al. 2018, their Fig. 10). The approximation also parallels the RC calibrations in *Gaia* bands that map M_G (Figure 6) as a function of color in (L. Ruiz-Dern et al. 2018) and the *Gaia*Unlimited example that selects RC stars by cutting around a fiducial RC ridge line in the *Gaia* CMD (Gaia Collaboration et al. 2018). Evolutionary states were utilized in the application of model-based large-separation corrections $f_{\Delta\nu}$, calculated using `asfgrid` interpolations over stellar-models as a function of evolutionary state, $T_{\rm eff}$, [Fe/H], and the raw $(\Delta\nu, \nu_{\rm max})$ (S. Sharma et al. 2016; D. Stello & S. Sharma 2023; S. Sharma et al. 2022).

To integrate our PySYD measurements into a community-average scale, we used the mean SYD-to-ensemble ratios $(X_{\Delta\nu}, X_{\nu_{\rm max}})$ from the APOKASC-3 inter-pipeline calibration and the sub-percent PySYD↔SYD consistency (M. H. Pinsonneault et al. 2025; A. Chontos et al. 2022b; S. Grusnis et al. 2025; C. Marasco et al. 2025).

We computed corrected parameters using

$$\Delta\nu_{\rm corr} = \frac{\Delta\nu_{\rm pySYD}}{X_{\Delta\nu}\, f_{\Delta\nu}},$$
$$\nu_{\rm max,corr} = \frac{\nu_{\rm max,pySYD}}{X_{\nu_{\rm max}}\, f_{\nu_{\rm max}}},$$

where $f_{\nu_{\rm max}}$ is a small adjustment derived by aligning seismic radii with *Gaia*-based radii after the $\Delta\nu$ scale is fixed. After observation of Figure 10, $f_{\nu_{\rm max}}$ is given a value of 1 since no meaningful correction was deemed necessary. This is consistent with our expectations for $f_{\nu_{\rm max}}$ around solar metallicity (C. J. Lindsay et al. 2025).

The corrected seismic parameters were then propagated through the standard scaling relations, with evolutionary-state dependent correction factors applied. Stellar radius and mass were computed as

$$\frac{R}{R_\odot} = \left(\frac{\nu_{\rm max,corr}}{\nu_{\rm max,\odot}}\right)\left(\frac{\Delta\nu_{\rm corr}}{\Delta\nu_\odot}\right)^{-2}\left(\frac{T_{\rm eff}}{T_{\rm eff,\odot}}\right)^{1/2},$$
$$\frac{M}{M_\odot} = \left(\frac{\nu_{\rm max,corr}}{\nu_{\rm max,\odot}}\right)^{3}\left(\frac{\Delta\nu_{\rm corr}}{\Delta\nu_\odot}\right)^{-4}\left(\frac{T_{\rm eff}}{T_{\rm eff,\odot}}\right)^{3/2}.$$

Here, $\nu_{\rm max,corr}$ and $\Delta\nu_{\rm corr}$ are the corrected parameters defined above, incorporating both the empirical SYD-to-ensemble calibration factors $(X_{\nu_{\rm max}}, X_{\Delta\nu})$ and the model-based $f_{\Delta\nu}$ correction together with the empirical $f_{\nu_{\rm max}}$ factor. The solar reference values $(\nu_{\rm max,\odot}, \Delta\nu_\odot, T_{\rm eff,\odot})$ adopted in this work are identical to those used in the APOKASC-3 calibration to maintain consistency across pipelines (M. H. Pinsonneault et al. 2025).

2.10. *Seismic Radii*

We determine stellar radii from asteroseismic scaling relations §2.9 with uncertainties from §2.13. For validation, we report them against external constraints. We use the *Gaia* DR3 *FLAME* catalog radii for red giants in the benchmark open cluster M67; these radii are derived from *Gaia* parallaxes and inferred angular diameters/stellar parameters (i.e., not seismic). The detailed *FLAME* comparison and our empirical re-calibration of radius uncertainties are presented in §2.13.2.

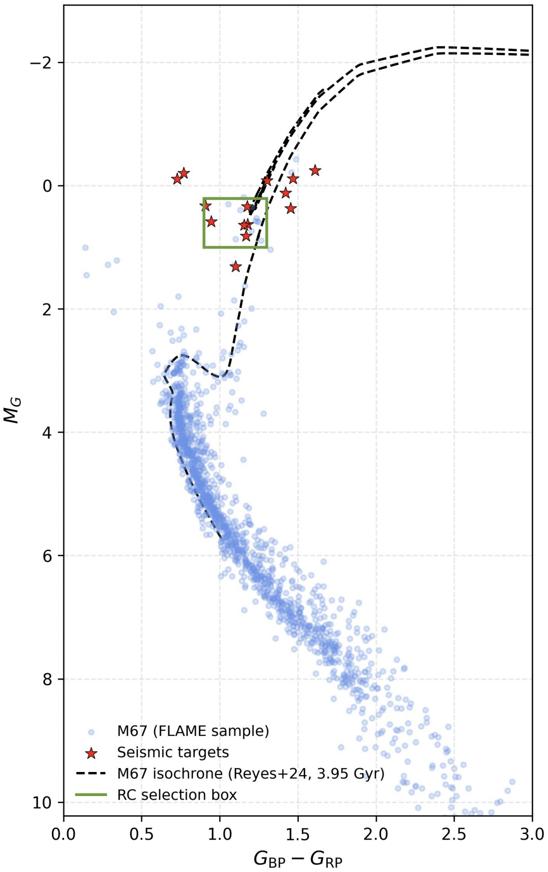

Figure 6. *Gaia* color–magnitude diagram of seismic targets from our sample (red stars) and the 3.95 Gyr M67 isochrone from C. Reyes et al. (2024); black dashed line) with the open cluster M67 overplotted for reference (blue points). The green box marks the adopted red clump (RC) selection region in ($G_{\rm BP} - G_{\rm RP}$) and M_G.

2.11. *Seismic Masses and Cluster-wise Reporting*

We determine stellar masses from asteroseismic scaling relations §2.9 with uncertainties from §2.13. For validation, we report the *seismic* mass distributions of three clusters (Casado Alessi-1, NGC 752, and Theia 6046), each target plotted against the masses of other members of the same cluster (Figure 11). This graphical analysis assesses internal, co-eval consistency rather than comparison to an external reference. In computing the cluster means and medians shown, we exclude the single Theia 6046 outlier (shown in Figure 11). Stars present in our broader sample but not confirmed as members of these three clusters are not plotted and do not enter the cluster-level statistics, but their seismic masses are included in the catalog.

2.12. *Stellar Age Estimation*

To estimate ages for our red giant cluster members, we use the age modeling tools in `Kiauhoku` (Z. R. Claytor 2020; Z. R. Claytor et al. 2020). The process compares each star to four different sets of stellar-evolution models following the multi-model strategy suggested by M. H. Pinsonneault et al. (2025), with the individual models taken from YREC (J. Tayar et al. 2022), Dartmouth/DSEP (A. Dotter et al. 2008), GARSTEC (A. Weiss & H. Schlattl 2008; A. M. Serenelli et al. 2013), and MIST (J. Choi et al. 2016). We use EEP-based tracks so that evolutionary stages are defined in a consistent way across all models. These models span the mass and metallicity ranges expected for our open clusters and let us test how different model assumptions affect red giant age estimates (L. M. Morales et al. 2025). For each star, we provide `Kiauhoku` with the observed quantities it can compare directly to the models: asteroseismic mass, $\log g$, and metallicity. `Kiauhoku` then interpolates within each model and computes a χ^2 measure of how well the model matches the observed values. These χ^2 values are turned into likelihood weights, and we construct an age distribution for each by marginalizing over the weighted models. We emphasize that, given the specific set of inputs provided to `Kiauhoku`, this procedure is a deterministic grid lookup and interpolation rather than a Bayesian inference. For the final age estimate of each star, we use MIST as our primary model. The Dartmouth, YREC and GARSTEC models are used as comparison models, and we report their mean ages to allow direct comparison with other work. Since different model families can give ages that differ (A. T. Theodoridis et al. 2025; J. Tayar et al. 2022; L. M. Morales et al. 2025; M. H. Pinsonneault et al. 2025), using multiple models provides an estimate of the model-dependent uncertainty. This systematic age uncertainty is then added in quadrature to the observational age uncertainty, which we infer by perturbing the input mass and metallicity by $\pm 1\sigma$ following the procedures of A. T. Theodoridis et al. (2025) and L. M. Morales et al. (2025).

2.12.1. *Cluster-Level Age Estimation*

For each star, the MIST stellar-evolution grid in `Kiauhoku` returns an age estimate t_i in Gyr. We define the cluster age as the arithmetic mean of the member-star ages,

$$\bar{t} = \frac{1}{N} \sum_{i=1}^{N} t_i. \qquad (2)$$

This quantity represents the characteristic red-giant age of the cluster as inferred from the MIST models, and we adopt $\bar{t}_{\rm MIST}$ as our final seismic cluster age.

2.13. *Error Propagation*

We propagated uncertainties with first-order partial-derivative error propagation, assuming independent inputs. We describe (i) how we defined the measurement uncertainties on $\nu_{\rm max}$ and $\Delta\nu$ from PySYD and by-eye checks, (ii) how these propagate into radius and mass and are tested against catalog radii, and (iii) how we constructed the final age error bars at both the stellar and cluster levels.

2.13.1. *Seismic Measurement Uncertainties from PySYD and By-Eye Checks*

For each star, we first measured $\nu_{\rm max}$ and $\Delta\nu$ with `PySYD` and then inspected the power spectra by eye to confirm that the reported peaks and uncertainties were reasonable. The adopted $\sigma_{\nu_{\rm max}}$ and $\sigma_{\Delta\nu}$ reflect the formal `PySYD` uncertainties, moderated by manual checks. Uncertainties in $T_{\rm eff}$, $\log g$, and [Fe/H] were taken directly from the relevant photometric or spectroscopic catalogs.

We treat $\nu_{\rm max}$, $\Delta\nu$, and $T_{\rm eff}$ as independent input quantities in the standard asteroseismic scaling relations. Using a first-order (Gaussian) Taylor expansion in $\ln X$. Applying standard error propagation yields the expressions below.

Seismic mass error propagation:

$$\left(\frac{\sigma_M}{M}\right)^2 = 9\left(\frac{\sigma_{\nu_{\rm max}}}{\nu_{\rm max}}\right)^2 + 16\left(\frac{\sigma_{\Delta\nu}}{\Delta\nu}\right)^2 + \frac{9}{4}\left(\frac{\sigma_{T_{\rm eff}}}{T_{\rm eff}}\right)^2$$

Seismic radius error propagation:

$$\left(\frac{\sigma_R}{R}\right)^2 = \left(\frac{\sigma_{\nu_{\rm max}}}{\nu_{\rm max}}\right)^2 + 4\left(\frac{\sigma_{\Delta\nu}}{\Delta\nu}\right)^2 + \frac{1}{4}\left(\frac{\sigma_{T_{\rm eff}}}{T_{\rm eff}}\right)^2$$

Seismic surface gravity error propagation:

$$\left(\frac{\sigma_g}{g}\right)^2 = \left(\frac{\sigma_{\nu_{\rm max}}}{\nu_{\rm max}}\right)^2 + \frac{1}{4}\left(\frac{\sigma_{T_{\rm eff}}}{T_{\rm eff}}\right)^2$$

2.13.2. *FLAME-Based Radius Error Calibration*

To validate our seismic radius scale and calibrate realistic radius uncertainties, we compare the scaling–relation radii to *Gaia* DR3 *FLAME* catalog values (Gaia Collaboration 2022). In the benchmark open cluster M67, the published *FLAME* radii for 18 coeval giants show a residual distribution compared to the radii in C. Reyes et al. (2024), where we plot $(R_{\rm seis} - R_{FLAME})/\sigma_{FLAME}$ for M67 giants. The broad and asymmetric shape of this distribution represents underestimated uncertainties in the *FLAME* radii. To promote realistic radius errors in our analysis, we adopt an uncertainty of $\pm 2.0\,\sigma$ of the *FLAME*-reported uncertainty for red-giant radii. This data-driven treatment of the scatter provides the most straightforward and conservative set of error bars while remaining consistent with our seismically derived radius estimates. Because these systematics are significant, we regard the C. Reyes et al. (2024) seismic radii as the most accurate and up-to-date radius determinations available for these stars, and we use them as our reference scale.

2.13.3. *Age Uncertainties at the Stellar and Cluster Levels*

For each star, we define age uncertainties by rerunning the `Kiauhoku` fits after shifting the input mass and metallicity by their $\pm 1\sigma$ errors. The resulting changes in the recovered ages capture the observational contribution to the age error (through mass and metallicity). We then add in quadrature the spread in age between the different stellar-evolution grids at fixed star to account for model dependence. The stellar age uncertainty can be written as

$$\sigma^2_{t,\star} = \sigma^2_{\rm obs} + \sigma^2_{\rm model}, \tag{3}$$

where $\sigma_{\rm obs}$ comes from perturbing the input mass and metallicity and $\sigma_{\rm model}$ reflects the grid-to-grid dispersion for that star. These $\sigma_{t,\star}$ values set the error bars on all star-by-star age plots. At the cluster level, the MIST grid provides a single mean age for the member stars (Section 2.12.1) and an associated uncertainty that reflects both the typical stellar age errors and the scatter of ages within the cluster. We therefore adopt the MIST cluster age, $t_{\rm MIST}$, as our final seismic age and assign an uncertainty

$$\sigma^2_{\rm MIST} = \frac{1}{N^2}\sum_{i=1}^{N}\sigma_i^2 + s^2_{\rm star}, \tag{4}$$

where σ_i is the age uncertainty for star i, and $s_{\rm star}$ is the sample-standard deviation of the member-star ages. In practice, the quoted $t_{\rm MIST} \pm \sigma_{\rm MIST}$ captures both uncertainty in the stellar inputs and the intrinsic spread of inferred ages within each cluster.

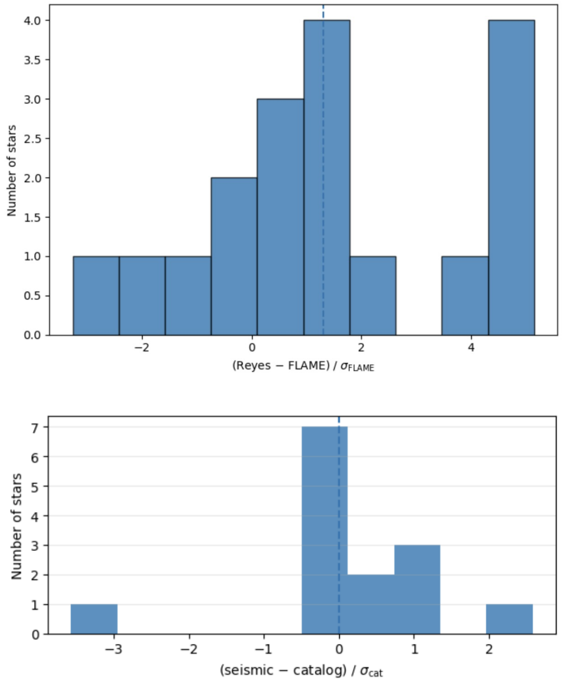

Figure 7. Normalized seismic–*FLAME* radius differences for M67. The upper panel reproduces the *FLAME*–asteroseismic comparison from C. Reyes et al. (2024), while the lower panel shows our own comparison using the same *FLAME* radii. In both cases, the distribution of $(R_{\rm seis} - R_{FLAME})/\sigma_{FLAME}$ demonstrates the large disparity between the *FLAME* radii and motivates our adoption of a conservative $\pm 2\sigma$ uncertainty for the radii of the stars studied here.

3. ANALYSIS

3.1. *Catalog Presentation*

We begin by presenting the full sample of stars selected for this study, including their basic astrometric and spectroscopic parameters. The catalog is constructed from *Gaia* DR3 and cross-matched with *TESS* Input Catalog identifiers. We illustrate the sample in a color–magnitude diagram (CMD) as a consistency check in Figure 1. This catalog includes columns which indicate whether or not a target has “passed” each cut, marked with ”y” for yes and ”n” for no. They are organized so that targets with the most “y”s are at the top and the least at the bottom, ensuring simplicity when searching for high quality targets. The full machine-readable catalog is available on Zenodo.

3.1.1. *Unknown Clusters*

The clusters marked as ”Unknown 1” (TIC306552754) and ”Unknown 2” (TIC306552795) in the catalog were both designated as ”Casado Alessi-1” in the E. L. Hunt & S. Reffert (2023) paper, but upon examination of another focused cluster membership study (T. Cantat-Gaudin & F. Anders 2020), we determined that they are likely non-members. A third source, ”Unknown 3” (TIC459055617), originally tagged as an NGC 2682 (M67) member, is likewise treated as a non-member because its properties are inconsistent with the confirmed M67 giants characterized by C. Reyes et al. (2025). However, all three objects have strong asteroseismic signals and are thus reported in the table.

Table 1. Description of columns in the machine-readable stellar catalog.

Column	Description	Unit	Example
TICID	*TESS* Input Catalog identifier	· · ·	306345133
GaiaDR3	*Gaia* DR3 source identifier	· · ·	2990380948461581056
cluster_name	Adopted cluster name	· · ·	Theia_6046
RA_ICRS	Right ascension (ICRS, *Gaia* DR3)	deg	78.5951
DE_ICRS	Declination (ICRS, *Gaia* DR3)	deg	-9.7912
pmRA	Proper motion in right ascension (*Gaia* DR3)	mas yr^{-1}	1.93
pmDE	Proper motion in declination (*Gaia* DR3)	mas yr^{-1}	0.58
Plx	Parallax (*Gaia* DR3)	mas	1.28
Gmag	*Gaia* G magnitude	mag	10.33
BPmag	*Gaia* $G_{\rm BP}$ magnitude	mag	10.98
RPmag	*Gaia* $G_{\rm RP}$ magnitude	mag	9.56
Classification	Manual photometric class	· · ·	Potential Red Giant
Within1kpc	Flag: within 1 kpc (y/n)	· · ·	y
Mag< 13/*TESS*	Flag: *TESS* magnitude $<$ 13 (y/n)	· · ·	y
Giants	Flag: giant candidate (y/n)	· · ·	y
crowdbleedsec	Flag: any *TESS* sector with crowding/bleeding issues (y/n)	· · ·	y
Crowding	*TESS* crowding metric proxy	· · ·	2.5
Bleeding	*TESS* bleeding metric proxy	· · ·	4.5
# of Available Sector(s)	Number of *TESS* sectors with usable light curves	· · ·	5
teff_gspphot	*Gaia* GSP-Phot effective temperature	K	4703.2
logg_gspphot	*Gaia* GSP-Phot surface gravity	dex	2.58
mh_gspphot	*Gaia* GSP-Phot metallicity [M/H]	dex	0.24
teff_gspspec	*Gaia* GSP-Spec effective temperature	K	4448
logg_gspspec	*Gaia* GSP-Spec surface gravity	dex	2.01
mh_gspspec	*Gaia* GSP-Spec metallicity [M/H]	dex	0.25
cluster_prob	Adopted cluster membership probability	· · ·	0.386
numax_pysyd	PySYD $\nu_{\rm max}$ (raw)	μHz	22.2
numax_error_upper	Upper uncertainty on PySYD $\nu_{\rm max}$	μHz	1.49
numax_error_lower	Lower uncertainty on PySYD $\nu_{\rm max}$	μHz	1.49
numax_corr	$\nu_{\rm max}$ after applied corrections	μHz	22.22
dnu_pysyd	PySYD $\Delta\nu$ (raw)	μHz	2.37
dnu_error_upper	Upper uncertainty on PySYD $\Delta\nu$	μHz	0.0348
dnu_error_lower	Lower uncertainty on PySYD $\Delta\nu$	μHz	0.0348
fdnu_used	Adopted $f_{\Delta\nu}$ correction factor	· · ·	0.993

Table 1 *continued*

Table 1 *(continued)*

Column	Description	Unit	Example
fdnu_source	Source of $f_{\Delta\nu}$ correction	···	asf
dnu_corr	$\Delta\nu$ after applied corrections	μHz	2.35
PySYD_Quality	PySYD quality flag (good/ok/bad)	···	good
snr	Signal-to-noise ratio of detected power excess	···	16.1
evo_state	Adopted evolutionary state (RGB/RC)	···	RGB
cat_mass	*Gaia FLAME* mass	$M_\odot$	3.00
M_cat_error_upper	Upper error on *FLAME* mass	$M_\odot$	0.8
M_cat_error_lower	Lower error on *FLAME* mass	$M_\odot$	0.4
cat_mass_err_stated	Catalog-stated fractional mass error	···	0.0593
cat_radius	*Gaia FLAME* radius	$R_\odot$	10.76
R_cat_error_upper	Upper error on *FLAME* radius	$R_\odot$	0.50
R_cat_error_lower	Lower error on *FLAME* radius	$R_\odot$	0.50
cat_radius_err_stated	Catalog-stated fractional radius error	···	0.249
cat_met	*Gaia* metallicity [M/H]	dex	-0.05
cat_met_err	Error on *Gaia* metallicity	dex	0.0096
cat_logg	*Gaia* surface gravity	dex	2.2964
cat_logg_err_upper	Upper error on *Gaia* $\log g$	dex	0.425
cat_logg_err_lower	Lower error on *Gaia* $\log g$	dex	0.425
cat_teff	*Gaia* effective temperature	K	4575.6
cat_teff_error_upper	Upper error on *Gaia* $T_{\rm eff}$	K	70.9
cat_teff_error_lower	Lower error on *Gaia* $T_{\rm eff}$	K	70.9
logg_seis	Seismic surface gravity from scaling relations	dex	2.244
logg_seis_upper	Upper error on seismic $\log g$	dex	0.0294
logg_seis_lower	Lower error on seismic $\log g$	dex	0.0294
R_seis	Seismic radius from scaling relations	$R_\odot$	21.09
R_seis_error_upper	Upper error on seismic radius	$R_\odot$	1.56
R_seis_error_lower	Lower error on seismic radius	$R_\odot$	1.56
M_seis	Seismic mass from scaling relations	$M_\odot$	2.85
M_seis_error_upper	Upper error on seismic mass	$M_\odot$	0.60
M_seis_error_lower	Lower error on seismic mass	$M_\odot$	0.60
cluster	Flag: accepted cluster member (y/n)	···	y
Removed?	Flag: removed from final analysis sample (y/n)	···	n
age_gyr	Adopted cluster age for this star	Gyr	0.487
sigma_seis	Seismic age uncertainty term	Gyr	-0.114
sigma_grid	Grid-based age scatter term	Gyr	0.159
sigma_big	Total age uncertainty combining error terms	Gyr	0.196
age_minus1sigma	Cluster age at -1σ bound	Gyr	0.595
age_std_minus1sigma	Uncertainty on age_minus1sigma	Gyr	0.260
age_plus1sigma	Cluster age at $+1\sigma$ bound	Gyr	0.367
age_std_plus1sigma	Uncertainty on age_plus1sigma	Gyr	0.0813
age_MIST	Best-fitting age from MIST model	Gyr	0.517
age_Dartmouth	Best-fitting age from Dartmouth model	Gyr	0.809
age_GARSTEC	Best-fitting age from GARSTEC model	Gyr	0.860
age_YREC	Best-fitting age from YREC model	Gyr	0.829
age_cantat_2020	Literature $\log_{10}$(age/yr) from Cantat-Gaudin (2020)	dex	···
age_hunt_2023	Literature $\log_{10}$(age/yr) from Hunt & Reffert (2023)	dex	9.5806
age_cantat_Gyr	Cantat-Gaudin (2020) age converted to Gyr	Gyr	···
age_hunt_Gyr	Hunt & Reffert (2023) age converted to Gyr	Gyr	3.807
all_ages	List of all adopted literature ages	Gyr	[3.807]
age_std_lit	Standard deviation of ages in all_ages	Gyr	0.0
cluster_age_final	Cluster age considering all members	Gyr	0.525
cluster_age_err	Error on cluster age	Gyr	0.0788

3.2. $\Delta\nu$–$\nu_{\rm max}$ *Relation of the Quality-Selected Sample*

As part of our analysis, we examine the $\Delta\nu$–$\nu_{\rm max}$ relation for the stars that passed the crowding, bleeding, and sector-quality filters described in §2.5. The retained sample follows the expected trend in $\Delta\nu$ versus $\nu_{\rm max}$, with outliers largely removed by these cuts; however, non-passing objects are still in figures. This is displayed in Fig. 8 and confirms that the quality selection standards presented in this method preserve seismic scaling, reduce contamination, and identify true oscillating giants.

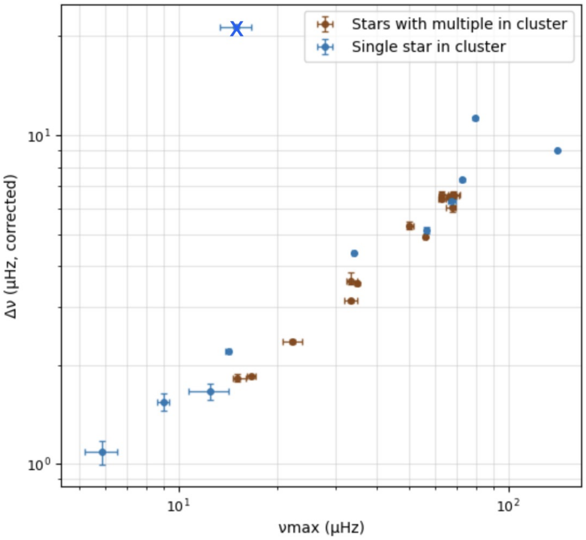

Figure 8. Corrected $\Delta\nu$ vs. $\nu_{\rm max}$. With the exception of a single outlier (marked as a blue "x"), our corrected $\Delta\nu$ values are strongly correlated with $\nu_{\rm max}$ in the expected way, indicating that the seismic parameters are reliable.

3.3. *Log g Comparison*

We validate surface gravity estimates by comparing spectroscopic $\log g$ with values inferred seismically via the $\nu_{\rm max}$ scaling relation, plotting $\log g_{\rm spec}$ against $\log g_{\rm seis}$ with uncertainties and a 1:1 reference line. On the full set ($N = 25$), we find a bias of +0.108 dex, median offset +0.015 dex, RMSE = 0.236 dex, robust spread $1.4826 \times$ MAD = 0.124 dex, and $R^2 = 0.744$, where MAD is the median absolute deviation. After removing two outliers using a MAD-z cut (with MAD-z defined as the absolute deviation from the median divided by $1.4826 \times$ MAD), the remaining $N = 23$ stars yield a bias of +0.065 dex, median offset −0.000 dex, RMSE = 0.167 dex, robust spread $1.4826 \times$ MAD = 0.112 dex, and $R^2 = 0.828$, indicating consistency between spectroscopic and seismic $\log g$.

3.4. *Radius Comparison*

Using the method outlined in §2.10, stellar radii are compared between seismic scaling-relation estimates and *Gaia*-based determinations. For each star, we use $\Delta\nu$, $\nu_{\rm max}$, and $T_{\rm eff}$ to compute $R_{\rm seis}$ and compare these values against the *FLAME* R_{Gaia} derived from *Gaia* parallaxes and bolometric corrections (Gaia Collaboration 2022). We quantify the agreement using fractional differences and dispersion, and present scatter plots with 1:1 reference lines to assess systematic offsets. On the full member set ($N = 13$), we find a bias of $+0.396\,R_\odot$, median offset $+0.165\,R_\odot$, RMSE = $5.165\,R_\odot$, robust spread $1.4826 \times$ MAD = $0.709\,R_\odot$, and $R^2 = -0.132$. After removing four outliers with a MAD-z cut, the remaining $N = 9$ targets yield a bias of $+0.082\,R_\odot$, median offset $+0.005\,R_\odot$, RMSE = $0.428\,R_\odot$, robust spread 1.4826×MAD = $0.469\,R_\odot$, and $R^2 = 0.992$, indicating consistency between seismic and *Gaia*-based radii and validating our choice to use $f_{\nu_{\rm max}} = 1$.

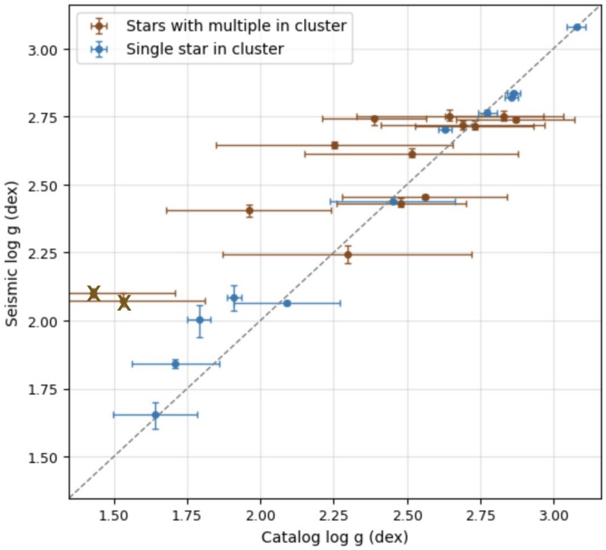

Figure 9. Seismic $\log g$ versus spectroscopic catalog $\log g$. The dashed line shows the 1:1 relation. With the exception of two outliers (marked as blue "x" symbols), our $\log g$ values inferred from the seismic $\nu_{\rm max}$ are strongly correlated with the spectroscopic $\log g$ values reported in the literature. We show only the $N = 23$ stars with literature spectroscopic $\log g$ measurements; the full set of 25 seismic $\log g$ values is given in Table 1.

3.5. *Mass Comparison*

Using the method described in §2.11, we present the seismic masses for all clusters in our sample. We report on the internal coherence of each cluster's mass distribution. In Figure 11, each cluster forms a generally tight cluster around a single mass. Each mass in our sample is derived independently from its own seismic observables and this type of coherence is expected for members of a coeval population.

3.6. *Stellar Age Validation*

As stated in §2.12, we adopt four independent sets of stellar-evolution models (YREC, Dartmouth/DSEP, GARSTEC, and MIST) and follow the multi-model strategy suggested by M. H. Pinsonneault et al. (2025). We use the dispersion among the four models to quantify the model-dependent component of the age uncertainty. For red clump stars, we assume no mass loss in the models when estimating ages, so the in-

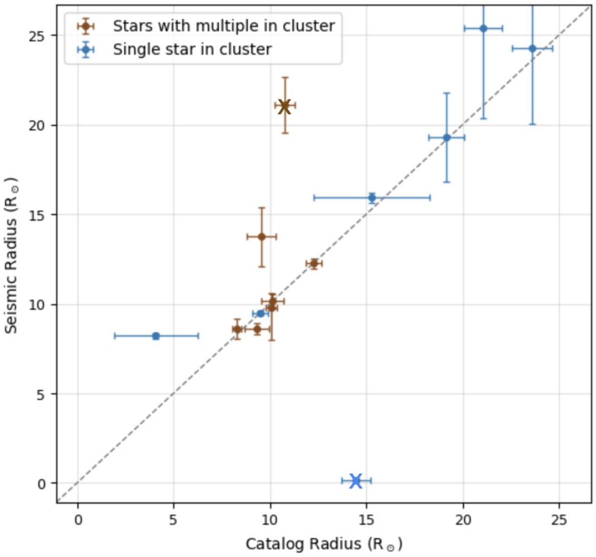

Figure 10. Seismic radius versus catalog radius with the 1:1 line shown as a dashed line. Error bars on the seismic radii reflect the uncertainties from our stellar age modeling, while error bars on the catalog radii use the adopted catalog radius uncertainties (including our inflated values, as described in §2.10).

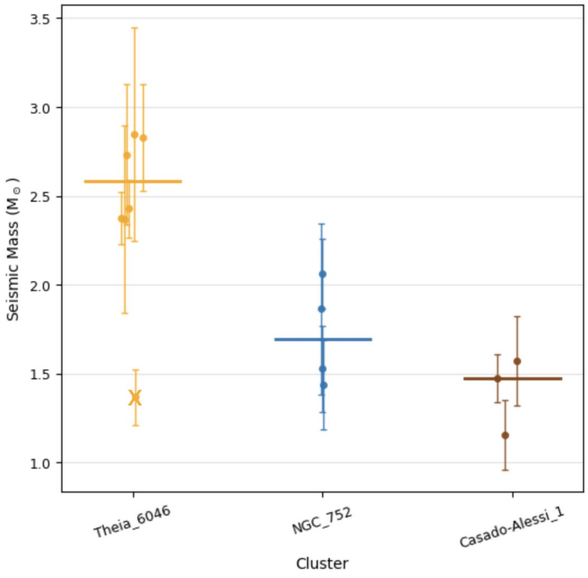

Figure 11. Seismic mass distributions by cluster with cluster medians (horizontal bars).

ferred ages correspond to stars that retain their initial masses, a reasonable limiting case for young clusters where mass loss is expected to be small (M. H. Pinsonneault et al. 2025).

Although our stars reside in clusters, not all of these clusters have a single well-determined age in the literature. For the 12 clusters with seismically inferred ages in this work, we compile the published ages and their spread in Table 3. Our model-based cluster ages are then compared to the mean literature ages, with error bars reflecting the literature scatter, in Figure 12. For all clusters, Figure 13 shows the distribution of stellar ages within each cluster relative to the corresponding literature value. In general, our results are consistent with literature values, although in some cases, our data show a preference for one group of ages over another. The level of internal consistency indicates that the method yields reliable cluster ages and supports its use as a basis for deriving ages of stars outside of clusters, where such calibrated seismic ages are particularly valuable for galactic-archaeology applications.

3.6.1. *Casado Alessi-1*

As shown in Figure 13, the interpolated ages for members of Casado Alessi-1 are not fully consistent with the literature range presented in past works. We were able to locate four age estimates for the cluster, 0.78, 0.8, 1.445, and 1.45 Gyr. Across our three estimations, the mean ages for Casado Alessi-1 are 1.63, 1.94, and 1.55 Gyr; in each case, the quoted 1σ error bars extend down into the 0.8–1.45 Gyr literature range, but the central values remain systematically higher. To explore this tension, we plot MIST isochrones of various ages on top of our catalog members of Casado Alessi-1, removing any targets that are outside of a 2σ window in parallax and proper motion around the adopted cluster means (or with RUWE $>$ 1.4) and may not be actual cluster members (Figure 14c). A discrepancy may arise from different membership selections or fitting choices in past or current work. Given our seismic uncertainties (Table 3) and analysis of isochrones compared to the cluster as a whole, we suspect that the age of this cluster may have been previously underestimated, but more detailed study is likely needed to solidify this age. We include Table 3 specifically to demonstrate that large per-star age uncertainties and grid-to-grid differences are common which makes the prevalence of error in cluster age determinations explicit. The full isochrone-fitting workflow for Casado Alessi-1 is available on GitHub.

3.6.2. *NGC 752*

As shown in Figure 13, the interpolated ages for members of NGC 752 are broadly consistent with the literature range reported in past work. Published ages for this nearby open cluster fall in the 1.3–1.6 Gyr range (T. Cantat-Gaudin & F. Anders 2020; E. L. Hunt & S. Reffert 2023). Our seismically derived ages for NGC 752 lie within this interval; in each case, the quoted 1σ error bars overlap the canonical literature range and the central values do not show any strong offset.

To further assess this agreement, we repeat the isochrone-based test used for Casado Alessi-1. In Figure 14a we plot *Gaia* DR3 color–magnitude data for likely members of NGC 752, removing stars that lie outside a 2σ window in parallax and proper motion around the adopted cluster means (or with RUWE $>$ 1.4), and marking the rejected targets with

Table 2. Compiled ages of the star clusters.

Cluster	Number of lit. age sources	Mean lit. age (Gyr)	Cantat-Gaudin (2020) age (Gyr)	Hunt & Reffert (2023) age (Gyr)	Seismic age (Gyr)
IC 348	8	0.005 ± 0.003	0.012	0.006	1.189 ± 0.309
Unknown 1	0	–	–	–	0.734 ± 0.280
Unknown 2	0	–	–	–	0.221 ± 0.237
LISC_3534	1	0.149	–	0.149	0.118 ± 0.752
COIN-*Gaia*_30	2	0.206 ± 0.052	0.257	0.154	4.251 ± 3.274
UPK 287	2	0.222 ± 0.060	0.257	0.154	0.667 ± 0.146
HSC_1052	1	0.068	0.068	–	0.108 ± 0.059
Unknown 3	0	–	–	–	6.405 ± 2.643
UPK 237	2	0.103 ± 0.048	0.151	0.055	0.262 ± 0.124
Casado Alessi-1	4	1.111 ± 0.337	1.445	0.749	1.706 ± 0.583
NGC 752	4	1.299 ± 0.166	1.175	1.421	1.433 ± 0.366
Theia 6046	1	3.807	–	3.807	0.525 ± 0.082

References: (1) S. E. Strom et al. (1974); (2) G. H. Herbig (1998); (3) E. Trullols & C. Jordi (1997); (4) K. E. Haisch et al. (2001); (5) C. J. Lada et al. (2006); (6) K. L. Luhman (1999); (7) E. H. Nikoghosyan et al. (2015); (10) E. L. Hunt & S. Reffert (2023); (12) R. Carrera et al. (2019); (13) A. Sarajedini (2009); (14) S. A. Barnes et al. (2016); (15) A. M. Geller et al. (2021); (16) G. Carraro et al. (1994); (17) S. M. Hassan (1972); (18) J. H. Peña & R. Peniche (1994); (19) H. M. Maitzen & H. Hensberge (1981); (20) C. Reyes et al. (2025)

Table 3. Ages and model comparisons for three Casado Alessi-1 giants.

TICID	age_gyr	age_std	age_gyr_-1σ	age_gyr_$+1\sigma$	age_MIST	age_Dartmouth	age_GARSTEC	age_YREC
306552813	1.627	0.811	2.254	1.127	1.843	2.746	2.469	2.299
306955660	1.944	0.905	2.748	1.261	2.169	2.950	2.479	2.301
306187638	1.547	0.780	2.203	1.150	1.764	2.689	2.465	2.297

red crosses. We overplot MIST isochrones with ages of 1.30, 1.40, 1.50, and 1.60 Gyr. The 1.3–1.5 Gyr isochrones provide a visibly good match to the main sequence, turnoff, and base of the red giant branch, reinforcing the conclusion that our seismic ages for NGC 752 are consistent with the literature values. The full isochrone-fitting workflow for NGC 752 is available on GitHub.

3.6.3. *Theia 6046*

As shown in Figure 13, the interpolated ages for members of Theia 6046 differ from the value reported in large catalog work. Hunt & Reffert (2023) give a cluster age of log $t \approx 9.58$ (roughly 3.8 Gyr), whereas our seismic estimation yields ages on the order of ~Gyr, substantially younger than this catalog value.

To explore this discrepancy, we repeat the isochrone-based test used for Casado Alessi-1 and NGC 752. In Figure 14b we plot *Gaia* DR3 color–magnitude data for likely members of Theia 6046, removing stars that lie outside a 2σ window in parallax and proper motion around the adopted cluster means (or with RUWE > 1.4), and marking the rejected targets with red crosses. We overplot MIST isochrones with ages of 0.3, 0.5, 0.7, 1.0, 1.5, and 3.7 Gyr. The younger ($\lesssim 1$ Gyr) isochrones provide a visibly better match to the main sequence and turnoff than the older ~ 3.7 Gyr track, suggesting that the true cluster age is likely younger than the catalog value. As with Casado Alessi-1, details of the membership selection and fitting methodology likely contribute to the discrepancy, but more detailed study is likely needed to solidify this age. The full isochrone-fitting workflow for Theia 6046 is available on GitHub.

4. CONCLUSION AND FUTURE WORK

We conclude that our method expands the available targets for asteroseismic analysis in star clusters using *TESS* light curves. We assembled a cluster-star catalog and workflow that integrates *Gaia* astrometry with *TESS* photometry to present red giants in clusters that are suitable for asteroseismic analysis. Our method (i) enforces distance, magnitude, and crowding/bleeding quality cuts, (ii) retrieves and preprocesses light curves, (iii) measures $\nu_{\rm max}$ and $\Delta\nu$ using PySYD, (iv) applies community and model-based corrections, (v) propagates uncertainties, (vi) validates radii, masses, and surface gravities across independent diagnostics, and (vii) compares our ages inferred from the asteroseismic analysis of red giants to the ages inferred in the literature from cluster CMDs. Our

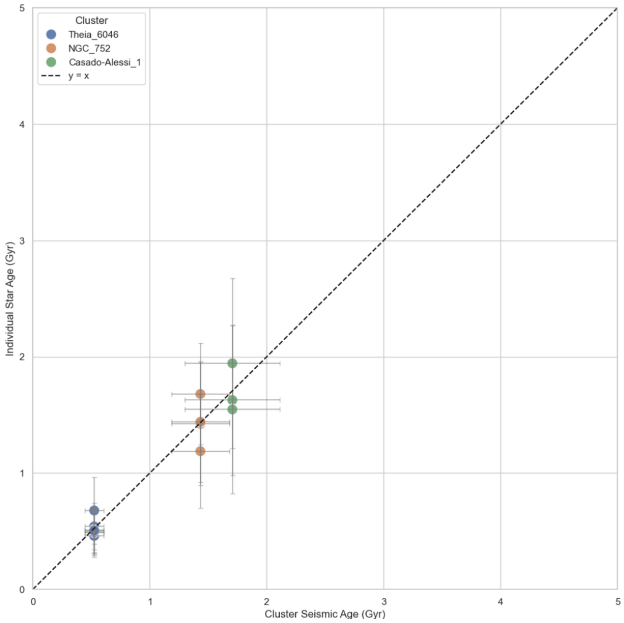

Figure 12. Individual star ages as a function of the corresponding cluster average age. Points are colored by cluster, with vertical error bars showing the uncertainty on each star's fitted age.

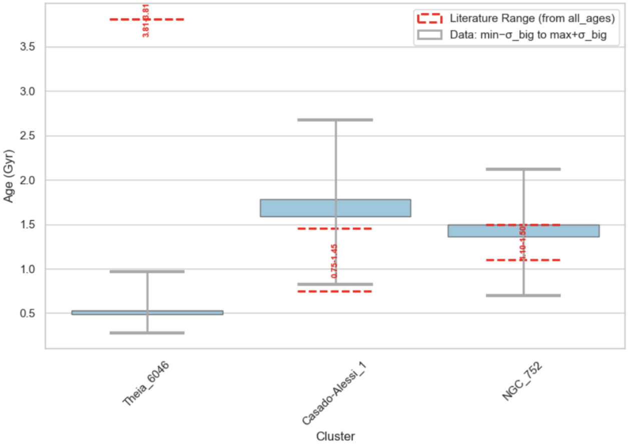

Figure 13. Boxplot of fitted ages for the clusters. Boxes represent the minimum-maximum age range in each cluster, whiskers show the full propagated uncertainty (age +/- error), and the bold line denotes the mean age. Red dashed lines indicate literature age estimates.

resulting catalogs, tables, cutouts, and notebooks provide a framework for expanding asteroseismology in clusters.

Our methodology is generally consistent with clusters having homogeneous ages. We show in Figure 12 that our independent ages for each star in the cluster are consistent in a way that allows us to combine estimates and infer cluster ages to a high degree of precision. We also show in Figure 13 that our ages are generally consistent with the literature ages for our clusters. We show in Figure 14 that, across NGC 752, Casado Alessi-1, and Theia 6046, the CMD-based isochrone fits can favor the catalog ages, the seismic ages, or strongly contradict the older catalog value in favor of a younger seismic solution. More generally, this suggests that asteroseismology can be a competitive way to infer cluster age, but that in many cases more detailed analysis of each cluster can be used to improve age estimates (C. Reyes et al. 2025). We view this paper primarily as a demonstration of the possibility of using *TESS*, even with its large pixel size and other limitations, to infer reliable cluster ages. We also hope that this analysis can serve as an initial step towards more detailed analysis of both individual stars and clusters in asteroseismic studies. We expect that additional spectroscopy (J. M. Otto et al. 2025), more advanced light-curve processing techniques (B. J. S. Pope et al. 2016), and individual mode analyses in clusters (C. J. Lindsay et al. 2025) would further tighten the constraints reported here. More generally, our work is intended as a contribution to a longer-term, community-wide effort to obtain robust asteroseismic mass and age estimates by combining stellar-evolution models and isochrones, detailed mode-by-mode asteroseismic analysis, comparisons to eclipsing binaries with dynamical masses, and the use of wide binaries and star clusters as coeval benchmarks (K. El-Badry et al. 2021; D. Godoy-Rivera & J. Chanamé 2018; J. Tayar & M. Joyce 2025; A. T. Theodoridis et al. 2025). Within this broader framework, the cluster-calibrated ages presented here help to cement asteroseismology as a precise and accurate technique for interpreting both exoplanetary systems and large galactic-archaeology samples such as APOGEE.

Clusters have long been our benchmarks for inferring stellar ages and calibrating other techniques. Our results suggest that ages inferred from asteroseismology can be reliable in clusters, and that more clusters are available to enhance calibration efforts. Looking ahead, space missions such as ESA's *PLATO* (H. Rauer et al. 2014) and NASA's *Roman* Space Telescope (M. A. Troxel et al. 2021) will offer the possibility of precise ages for hundreds of thousands of targets and extend this approach to even larger distances. To make full use of the precision of asteroseismology on such a broad scale, it is necessary to validate its accuracy against key calibration systems such as star clusters and wide binaries, and to compare it with other techniques over a range of ages and metallicities (A. Miglio et al. 2013, 2021a). Using tools like *Roman*, *PLATO*, and other dedicated missions (A. Miglio et al. 2021b) in this way will allow us to unlock the detailed evolutionary history of the Milky Way in a fully multidimensional sense.

ACKNOWLEDGMENTS

This work was supported by the University of Florida College of Liberal Arts and Sciences. C. Mankowski received course credit for this research through the Department of Astronomy. We thank J. Tayar for supervision and weekly discussions guiding the analysis. We acknowledge helpful

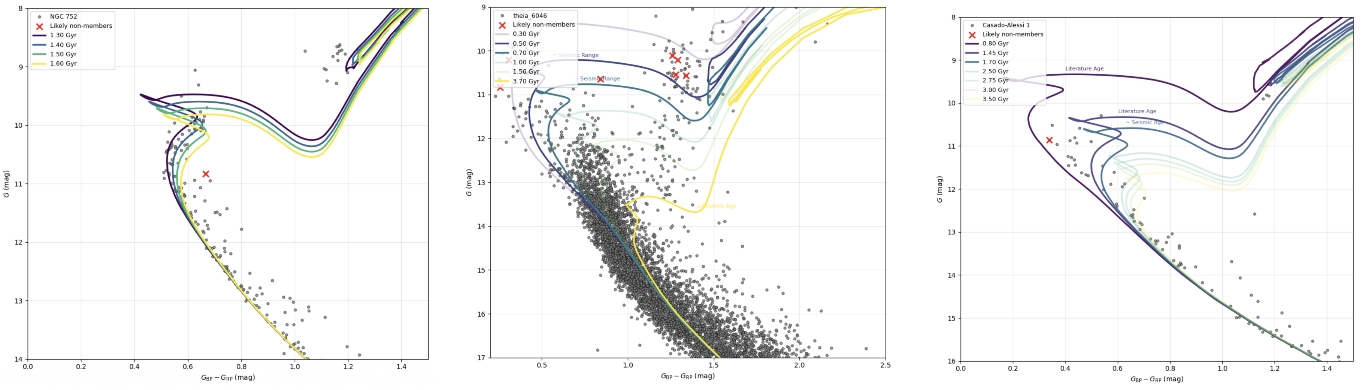

(a) NGC 752

(b) Theia 6046

(c) Casado Alessi 1

Figure 14. Color–magnitude diagrams for the open clusters NGC 752 (left), Theia 6046 (middle), and Casado Alessi 1 (right) using *Gaia* DR3 photometry. Grey points show likely cluster members; likely non-members are marked as red crosses. Colored curves are MIST isochrones at various ages plotted assuming an extinction $E(B-V)$ from (T. Cantat-Gaudin & F. Anders 2020) and a distance modulus of (E. L. Hunt & S. Reffert 2023).

assistance with `PySYD` from A. Beyer. We thank Y. Nouredine and C. Wagner for reading the manuscript and providing comments. This paper includes data collected by the *TESS* mission and obtained from the Mikulski Archive for Space Telescopes (MAST) at the Space Telescope Science Institute (STScI). The *TESS* mission is funded by NASA's Science Mission Directorate, and funding for *TESS* is provided by the NASA Explorer Program. STScI is operated by the Association of Universities for Research in Astronomy, Inc., under NASA contract NAS 5–26555. Some of the data presented in this paper were obtained from MAST. Support for MAST for non-HST data is provided by the NASA Office of Space Science via grant NAG5-7584 and by other grants and contracts.

This work has made use of data from the European Space Agency (ESA) mission *Gaia* (https://www.cosmos.esa.int/gaia), processed by the *Gaia* Data Processing and Analysis Consortium (DPAC, https://www.cosmos.esa.int/web/gaia/dpac/consortium). Funding for the DPAC has been provided by national institutions, in particular the institutions participating in the *Gaia* Multilateral Agreement.

AUTHOR CONTRIBUTIONS

C. Mankowski carried out all aspects of this project, including data compilation, target selection, light curve analysis, seismic parameter extraction, application of corrections, age fitting, figure generation, and manuscript preparation, with the exception of Section 2.5 of the Methods, which was written and performed by C. Martin. J. Tayar conceived the project through her original proposal, provided overall supervision, provided manuscript edits, and met with C. Mankowski weekly to discuss methodology, results, and interpretation.

SOFTWARE AND THIRD PARTY DATA REPOSITORY CITATIONS

This research made use of `astropy` (Astropy Collaboration et al. 2013, 2018, 2022), `lightkurve` (Lightkurve Collaboration 2018), `PySYD` (A. Chontos et al. 2022a), `asfgrid` (S. Sharma et al. 2016), `MIST` (J. Choi et al. 2016), `Dartmouth` (A. Dotter et al. 2008), `YREC` (P. Demarque et al. 2008), `GARSTEC` (A. Weiss & H. Schlattl 2008), and visualization and analysis packages including `numpy`, `pandas`, `scipy`, `matplotlib`, `Échelle` (D. Hey & W. H. Ball 2020), `Bokeh` (Bokeh Development Team 2018), `Panel`, `astroquery`, and `ebf`. This work was partially carried out in the TIKE (Time-series Integrated Knowledge Engine) environment provided by STScI/MAST.

We made use of data from the Mikulski Archive for Space Telescopes (MAST) for *TESS* observations, the ESA *Gaia* Archive for DR3 data.

REFERENCES

Andrae, R., Rix, H.-W., & Chandra, V. 2023, The Astrophysical Journal Supplement Series, 267, 8, doi: 10.3847/1538-4365/acd53e

Ash, A. L., Pinsonneault, M. H., Vrard, M., & Zinn, J. 2024, arXiv e-prints. https://arxiv.org/abs/2411.10520

Astropy Collaboration, Price-Whelan, A. M., Lim, P. L., et al. 2022, The Astrophysical Journal, 935, 167, doi: 10.3847/1538-4357/ac7c74

Astropy Collaboration, Price-Whelan, A. M., Sipőcz, B. M., et al. 2018, The Astronomical Journal, 156, 123, doi: 10.3847/1538-3881/aabc4f

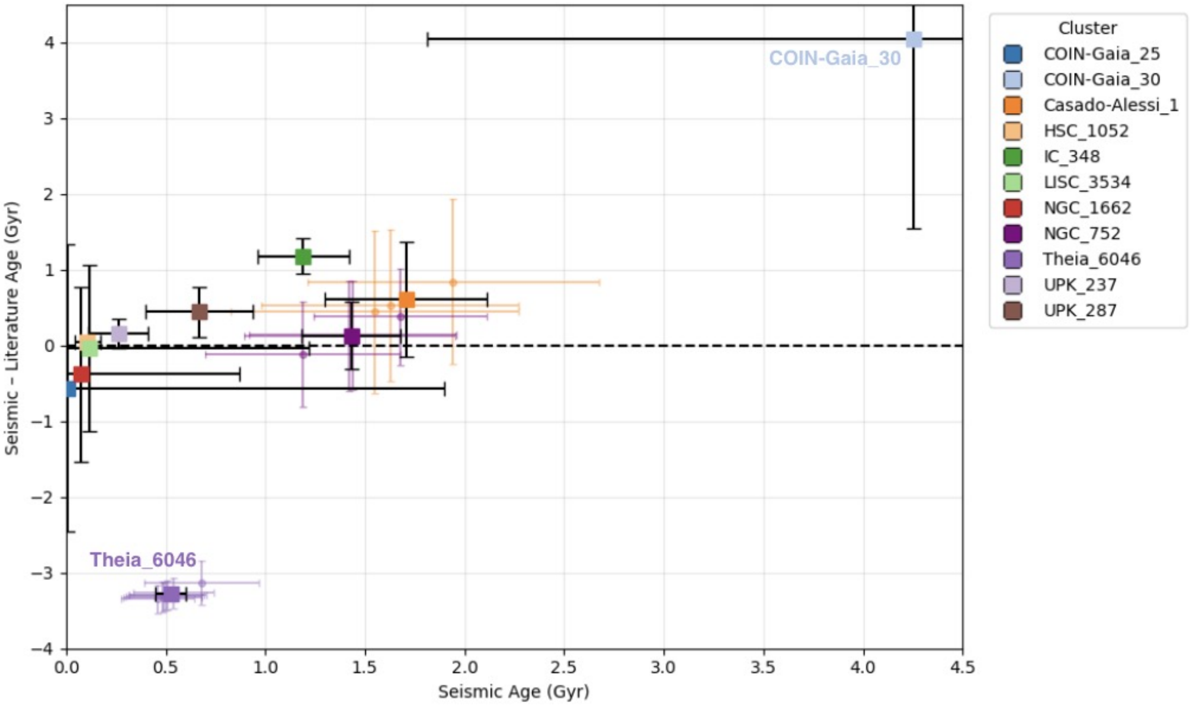

(a) All literature ages

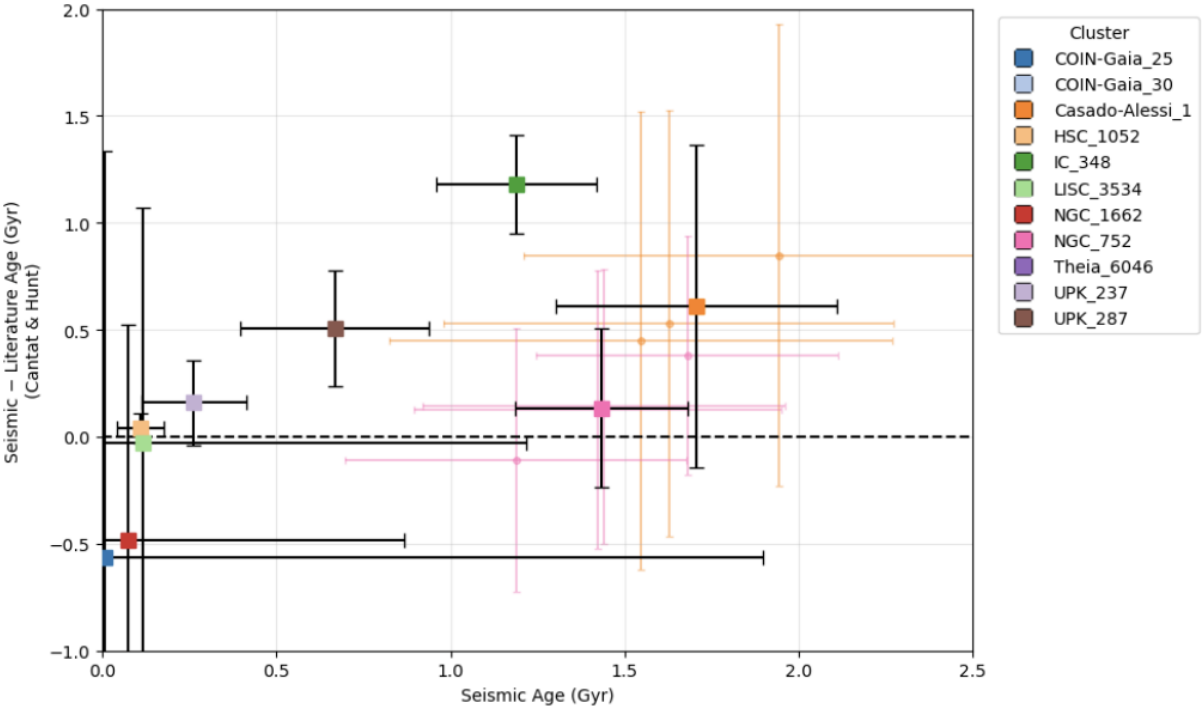

(b) Cantat-Gaudin (2020) and Hunt & Reffert (2023) only

Figure 15. Residual comparison between seismic ages and literature ages for all clusters in the sample. Cluster means are plotted as solid colors with black error bars. Clusters with more than one member have all members plotted behind it. In panel (a), the x-axis shows the seismic ages (Gyr) with their 1σ uncertainties, and the y-axis shows the difference between the seismic age and the central literature age. Panel (b) shows the same residuals, but using only the Cantat-Gaudin (2020) and Hunt & Reffert (2023) ages as the literature references. Panel (b) discludes Theia 6046 (discussed in §3.6.3) and outlier COIN-*Gaia* 30.

Astropy Collaboration, Robitaille, T. P., Tollerud, E. J., et al. 2013, Astronomy & Astrophysics, 558, A33, doi: 10.1051/0004-6361/201322068

Baglin, A., Auvergne, M., Barge, P., et al. 2006, The Publications of the Astronomical Society of the Pacific, 118, 140, doi: 10.1086/500210

Barclay, T., Burke, C. J., Catanzarite, J., et al. 2020, arXiv e-prints. https://arxiv.org/abs/2002.01502

Barnes, S. A., Weingrill, J., Fritzewski, D., Strassmeier, K. G., & Platais, I. 2016, ApJ, 823, 16, doi: 10.3847/0004-637X/823/1/16

Bokeh Development Team. 2018,, Astrophysics Source Code Library

Borucki, W. J., Koch, D., Basri, G., et al. 2010, Science, 327, 977, doi: 10.1126/science.1185402

Boyle, A. W., Mann, A. W., & Bush, J. 2025, The Astrophysical Journal, 985, 233

Brown, T. M., Christensen-Dalsgaard, J., Dziembowski, W. A., et al. 1989, The Astrophysical Journal, 343, 526

Buder, S., Sharma, S., Kos, J., et al. 2021, Monthly Notices of the Royal Astronomical Society, 506, 150, doi: 10.1093/mnras/stab1242

Cantat-Gaudin, T., & Anders, F. 2020, Astronomy & Astrophysics, 633, A99, doi: 10.1051/0004-6361/201936691

Carraro, G., Chiosi, C., Bressan, A., & Bertelli, G. 1994, A&AS, 103, 375

Carrera, R., Pasquato, M., Vallenari, A., et al. 2019, arXiv preprint arXiv:1905.02020. https://arxiv.org/abs/1905.02020

Casali, G., Magrini, L., Tautvaišienė, G., et al. 2022, Astronomy & Astrophysics, 666, A180, doi: 10.1051/0004-6361/202244180

Chaplin, W. J., & Miglio, A. 2013, Annual Review of Astronomy and Astrophysics, 51, 353, doi: 10.1146/annurev-astro-082812-140938

Choi, J., Dotter, A., Conroy, C., et al. 2016, The Astrophysical Journal, 823, 102, doi: 10.3847/0004-637X/823/2/102

Chontos, A., Huber, D., Beyer, A., et al. 2022a,, https://github.com/ashleychontos/pysyd

Chontos, A., Huber, D., Sayeed, M., & Yamsiri, P. 2022b, Journal of Open Source Software, 7, 3331, doi: 10.21105/joss.03331

Claytor, Z. R. 2020, https://ascl.net/2011.027

Claytor, Z. R., van Saders, J. L., Santos, Á. R. G., et al. 2020, The Astrophysical Journal, 888, 43, doi: 10.3847/1538-4357/ab5c24

Cowan, J. J., Sneden, C., Lawler, J. E., et al. 2025, Universe, 11, 229, doi: 10.3390/universe11070229

Demarque, P., Guenther, D. B., Li, L., Mazumdar, A., & Straka, C. W. 2008, Astrophysics and Space Science, 316, 31, doi: 10.1007/s10509-007-9837-1

Donor, J., Cunha, K., Frinchaboy, P. M., et al. 2023, arXiv e-prints. https://arxiv.org/abs/2206.13650

Dotter, A., Chaboyer, B., Jevremović, D., et al. 2008, The Astrophysical Journal Supplement Series, 178, 89, doi: 10.1086/589654

El-Badry, K., Rix, H.-W., & Heintz, T. M. 2021, Monthly Notices of the Royal Astronomical Society, 506, 2269, doi: 10.1093/mnras/stab323

Elsworth, Y., Hekker, S., Johnson, J. A., et al. 2019, Monthly Notices of the Royal Astronomical Society, 489, 4641, doi: 10.1093/mnras/stz2356

Fausnaugh, M., & the TESS Team. 2023,, Tech. Rep. DR84, TESS Science Office. https://tasoc.dk/docs/release_notes/tess_sector_59_drn84_v02.pdf

Feuillet, D. K., Bovy, J., Holtzman, J., et al. 2018, Monthly Notices of the Royal Astronomical Society, 477, 2326, doi: 10.1093/mnras/sty779

Gai, M., Vecchiato, A., Riva, A., et al. 2022, arXiv e-prints. https://arxiv.org/abs/2212.02357

Gaia Collaboration. 2022,, Gaia DPAC documentation, Astrophysical Parameters Supplement (gaiadr3.astrophysical_parameters_supp)

Gaia Collaboration, Babusiaux, C., van Leeuwen, F., et al. 2018, Astronomy & Astrophysics, 616, A10, doi: 10.1051/0004-6361/201832843

Gaia Collaboration, Brown, A. G. A., Vallenari, A., et al. 2023, Astronomy & Astrophysics, 674, A1, doi: 10.1051/0004-6361/202243940

García, R. A., Montalbán, J., Miglio, A., & Mathur, S. 2022, Nature Astronomy, 6, 1234, doi: 10.1038/s41550-022-01713-2

Geller, A. M., Mathieu, R. D., Latham, D. W., et al. 2021, AJ, 161, 190, doi: 10.3847/1538-3881/abdd23

Godoy-Rivera, D., & Chanamé, J. 2018, Monthly Notices of the Royal Astronomical Society, 479, 4440, doi: 10.1093/mnras/sty1737

Grusnis, S., Tayar, J., & Godoy-Rivera, D. 2025, arXiv e-prints. https://arxiv.org/abs/2509.12513

Guerrero, N. M., et al. 2021, The Astrophysical Journal Supplement Series, 254, 39

Haisch, Jr., K. E., Lada, E. A., & Lada, C. J. 2001, AJ, 121, 2065, doi: 10.1086/319951

Hassan, S. M. 1972, Mem. Soc. Astron. Italiana, 43, 117

Hatt, E., Nielsen, M. B., Chaplin, W. J., et al. 2023, Astronomy & Astrophysics, 669, A67, doi: 10.1051/0004-6361/202243064

Hekker, S., Gilliland, R. L., Elsworth, Y., et al. 2011, Monthly Notices of the Royal Astronomical Society, 414, 2594, doi: 10.1111/j.1365-2966.2011.18526.x

Herbig, G. H. 1998, ApJ, 497, 736, doi: 10.1086/305500

Hey, D., & Ball, W. 2020,, 1.4 Zenodo, doi: 10.5281/zenodo.3629933

Hey, D., & Ball, W. H. 2020, Journal of Open Source Software, 5, 2051, doi: 10.21105/joss.02051

Hon, M., Stello, D., & Zinn, J. C. 2021, The Astrophysical Journal Supplement Series, 254, 41, doi: 10.3847/1538-4365/abe86a

Hon, M., Kuszlewicz, J. S., Stello, D., et al. 2022, The Astrophysical Journal Supplement Series, 262, 14, doi: 10.3847/1538-4365/ac8003

Hon, M., Stello, D., Zinn, J. C., et al. 2024, The Astrophysical Journal, 950, 112, doi: 10.3847/1538-4357/ad25d2

Horta, D., Lu, Y., Ness, M. K., Lisanti, M., & Price-Whelan, A. M. 2024, The Astrophysical Journal, 971, 170, doi: 10.3847/1538-4357/ad58de

Howell, S. B., Sobeck, C., Haas, M., et al. 2014, Publications of the Astronomical Society of the Pacific, 126, 398, doi: 10.1086/676406

Huber, D., et al. 2009, Communications in Asteroseismology, 160, 74. https://ui.adsabs.harvard.edu/abs/2009CoAst.160...74H/

Hunt, E. L., & Reffert, S. 2023, Astronomy & Astrophysics, 673, A114, doi: 10.1051/0004-6361/202346285

Hunt, E. L., & Reffert, S. 2023, A&A, 673, A114, doi: 10.1051/0004-6361/202346285

Jenkins, J. M., Twicken, J. D., McCauliff, S., et al. 2016, Proceedings of the SPIE, 9913, 99133E, doi: 10.1117/12.2233418

Kjeldsen, H., & Bedding, T. R. 1995, Astronomy and Astrophysics, 293, 87

Konchady, T. 2020,, AAS Nova https://aasnova.org/2020/08/21/getting-deeper-into-hr-diagrams-with-gaia/

Lada, C. J., Muench, A. A., Luhman, K. L., et al. 2006, AJ, 131, 1574, doi: 10.1086/499808

Lebreton, Y., & Montalbán, J. 2008, Proceedings of the International Astronomical Union, 4, 419, doi: 10.1017/S1743921309032074

Lightkurve Collaboration. 2018,, https://docs.lightkurve.org

Lindegren, L., et al. 2018, Astronomy & Astrophysics, 616, A2, doi: 10.1051/0004-6361/201832727

Lindsay, C. J., Hon, M., Ong, J. M. J., et al. 2025, The Astrophysical Journal. https://arxiv.org/abs/2507.01091

Lu, Y., Angus, R., Agüeros, M. A., et al. 2020, The Astronomical Journal, 160, 207, doi: 10.3847/1538-3881/abada4

Luhman, K. L. 1999, ApJ, 525, 466, doi: 10.1086/307902

Lund, M. N., Handberg, R., Davies, G. R., et al. 2021, The Astrophysical Journal Supplement Series, 257, 53, doi: 10.3847/1538-4365/ac143f

Maitzen, H. M., & Hensberge, H. 1981, A&A, 96, 151

Marasco, C., Tayar, J., & Nidever, D. 2025, The Astrophysical Journal, 986, 144

Miglio, A., Chiappini, C., Morel, T., et al. 2013, Monthly Notices of the Royal Astronomical Society, 429, 423, doi: 10.1093/mnras/sts345

Miglio, A., Girardi, L., Grundahl, F., et al. 2021a, Experimental Astronomy, 51, 963, doi: 10.1007/s10686-021-09711-1

Miglio, A., Chiappini, C., Mosser, B., et al. 2021b, Astronomy & Astrophysics, 645, A85, doi: 10.1051/0004-6361/202039656

MIT TESS Science Office. 2025,, https://tess.mit.edu/qlp/

Morales, L. M., Tayar, J., & Claytor, Z. R. 2025, The Astrophysical Journal, 986, 229, doi: 10.3847/1538-4357/add2f5

Mosser, B., Michel, E., Belkacem, K., & Samadi, R. 2018, in Handbook of Exoplanets, ed. H. J. Deeg & J. A. Belmonte (Springer), 1–32, doi: 10.1007/978-3-319-55333-7_116

Mosser, B., Elsworth, Y., Hekker, S., et al. 2012, Astronomy & Astrophysics, 537, A30, doi: 10.1051/0004-6361/201117352

Murphy, S. J. 2015, Monthly Notices of the Royal Astronomical Society, 453, 2569, doi: 10.1093/mnras/stv1842

Nikoghosyan, E. H., Vardanyan, A. V., & Khachatryan, K. G. 2015, Astrophysics, 58, 490, doi: 10.1007/s10511-015-9402-9

Otto, J. M., Frinchaboy, P. M., Myers, N. R., et al. 2025, The Astronomical Journal. https://arxiv.org/abs/2507.07264

Palakkatharappil, D. B., & Creevey, O. L. 2023, Astronomy & Astrophysics, 672, A123, doi: 10.1051/0004-6361/202243624

Peña, J. H., & Peniche, R. 1994, RMxAA, 28, 139

Pinsonneault, M. H., Zinn, J. C., Tayar, J., et al. 2025, The Astrophysical Journal Supplement Series, 276, 69, doi: 10.3847/1538-4365/ad9fef

Pope, B. J. S., White, T. R., Huber, D., et al. 2016, Monthly Notices of the Royal Astronomical Society: Letters, 455, L36, doi: 10.1093/mnrasl/slv143

Rauer, H., Catala, C., Aerts, C., et al. 2014, Experimental Astronomy, 38, 249, doi: 10.1007/s10686-014-9383-4

Reyes, C., Casamiquela, L., Anders, F., et al. 2024, Monthly Notices of the Royal Astronomical Society, 532, 2860, doi: 10.1093/mnras/stae1650

Reyes, C., Stello, D., Hon, M., et al. 2025, Monthly Notices of the Royal Astronomical Society, 538, 1720, doi: 10.1093/mnras/staf353

Ricker, G. R., Winn, J. N., Vanderspek, R., et al. 2015, Journal of Astronomical Telescopes, Instruments, and Systems, 1, 014003, doi: 10.1117/1.JATIS.1.1.014003

Riello, M., De Angeli, F., Evans, D. W., et al. 2021, Astronomy & Astrophysics, 649, A3, doi: 10.1051/0004-6361/202039587

Risbud, S., Carraro, G., & Boffin, H. M. J. 2025, arXiv e-prints. https://arxiv.org/abs/2501.17225

Ruiz-Dern, L., Babusiaux, C., Arenou, F., Turon, C., & Lallement, R. 2018, Astronomy and Astrophysics, 609, A116, doi: 10.1051/0004-6361/201731572

Sarajedini, A. 2009, arXiv preprint arXiv:0904.2907. https://arxiv.org/abs/0904.2907

Schiavon, R. P., Johnson, C. I., Holtzman, J. A., et al. 2023, Monthly Notices of the Royal Astronomical Society, 528, 1393, doi: 10.1093/mnras/stad471

Serenelli, A. M., Bergemann, M., Ruchti, G., & Casagrande, L. 2013, Monthly Notices of the Royal Astronomical Society, 429, 3645, doi: 10.1093/mnras/sts648

Sharma, S., Stello, D., Bland-Hawthorn, J., Huber, D., & Bedding, T. R. 2016, The Astrophysical Journal, 822, 15, doi: 10.3847/0004-637X/822/1/15

Sharma, S., Stello, D., Zinn, J. C., et al. 2022, Monthly Notices of the Royal Astronomical Society, 517, 1970, doi: 10.1093/mnras/stac2031

Stassun, K. G., Oelkers, R. J., Pepper, J., & et al. 2019a,, MAST—Mikulski Archive for Space Telescopes

Stassun, K. G., Oelkers, R. J., Paegert, M., et al. 2019b,, VizieR Online Data Catalog

Stassun, K. G., Oelkers, R. J., Paegert, M., et al. 2019c, The Astronomical Journal, 158, 138, doi: 10.3847/1538-3881/ab3467

Stello, D., & Sharma, S. 2023, https://arxiv.org/abs/2305.03221

Strom, S. E., Strom, K. M., & Carrasco, L. 1974, PASP, 86, 798, doi: 10.1086/129676

Tayar, J., Claytor, Z. R., Huber, D., & van Saders, J. 2022, The Astrophysical Journal, 927, 31, doi: 10.3847/1538-4357/ac4bbc

Tayar, J., & Joyce, M. 2025, The Astrophysical Journal Letters, 984, doi: 10.3847/2041-8213/adcd6f

TESS Science Processing Operations Center. 2025,, Tech. rep., NASA Ames Research Center. https://tasoc.dk/docs/release_notes/tess_sector_82_drn115_v01.pdf

Theodoridis, A. T., Morales, L., & Tayar, J. 2025, arXiv e-prints, arXiv:2505.08109, doi: 10.48550/arXiv.2505.08109

Thomas, D., Maraston, C., Bender, R., & Mendes de Oliveira, C. 2005, The Astrophysical Journal, 621, 673, doi: 10.1086/426932

Troxel, M. A., Long, H., Hirata, C. M., et al. 2021, Monthly Notices of the Royal Astronomical Society, 501, doi: 10.1093/mnras/staa3658

Trullols, E., & Jordi, C. 1997, A&A, 324, 549

Vrard, M., Pinsonneault, M. H., Elsworth, Y., et al. 2025, Astronomy & Astrophysics, 697, A165, doi: 10.1051/0004-6361/202452635

Weiss, A., & Schlattl, H. 2008, Astrophysics and Space Science, 316, 99, doi: 10.1007/s10509-007-9606-5

Xiang, M., Ting, Y.-S., Rix, H.-W., Stello, D., et al. 2023, Monthly Notices of the Royal Astronomical Society, 523, 3456, doi: 10.1093/mnras/stad1300

Yang, J.-Y., Chen, D.-C., Xie, J.-W., et al. 2023, arXiv e-prints, doi: 10.48550/arXiv.2310.20113

Ying, J. M., Chaboyer, B., Boylan-Kolchin, M., Weisz, D., & Goebel-Bain, R. 2025, The Astrophysical Journal, doi: 10.48550/arXiv.2505.02969

Yu, J., Huber, D., Bedding, T. R., et al. 2018, The Astrophysical Journal Supplement Series, 236, 42, doi: 10.3847/1538-4365/aabfd0

Zhou, J., Bi, S., Yu, J., et al. 2024, The Astrophysical Journal Supplement Series, 271, 17, doi: 10.3847/1538-4365/ad18db

Zinn, J. C., Stello, D., Elsworth, Y., et al. 2022, The Astrophysical Journal, 926, 191, doi: 10.3847/1538-4357/ac2c83